Physics of the Earth and Planetary Interiors 344 (2023) 107107

Contents lists available at ScienceDirect

Physics of the Earth and Planetary Interiors

journal homepage: www.elsevier.com/locate/pepi

Crustal structure and isostatic compensation beneath the South China Sea using satellite gravity data and its implications for the rifting and magmatic activities

A.V. Satyakumar [a,*], Shuanggen Jin [b,c], Virendra M. Tiwari [a], Songbai Xuan [b]

[a] CSIR-National Geophysical Research Institute, Uppal Road, Hyderabad 500007, India
[b] Shanghai Astronomical Observatory, Chinese Academy of Sciences, Shanghai 200030, China
[c] School of Surveying and Land Information Engineering, Henan Polytechnic University, Jiaozuo 454003, China

ARTICLE INFO

Keywords:
South China Sea
Satellite gravity
Isostasy
Crustal structure
Geoid-topography ratio
Vertical tectonic stress

ABSTRACT

Opening of the South China Sea (SCS) was triggered by the breakup of south-eastern Eurasia and the southward drifting of the Palawan-Reed Bank microcontinent, as various prior studies have suggested. The young, moderately magmatic, rifted northern margin of the SCS is vital for investigating the relationship among magmatism, rheology, and structural evolution. This paper integrates satellite gravity anomaly, elevation/bathymetry, geoid, and seismic velocities to investigate continental breakup, magmatism, and rifting beneath the South China Sea. Source depths of 146, 31.5, and 8 km derived from the spectrum of Bouguer gravity anomalies suggest the average depths of the lithospheric base, continental, and oceanic crustal bases, respectively. Correspondingly, gravity Moho ranges from 8 km beneath the rifting center of SCS to 42 km in the Indo-China block. It is worth mentioning that the isostatic Moho from the Airy and flexural models were highly correlated with gravity Moho with correlation coefficients of ~1. From the ratio between geoid and topography and our estimate of the vertical tectonic stress, the seamounts and reefs (Shuangfeng Basin: SB, Reed Bank: RB, Macclesfield Bank: MB) have a deep compensation depth. In contrast, the other parts (Manila Trench: MT, Phu Khan Basin: PK, East Sub Basin: ESB) have a smaller depth of compensation. 2D gravity modelling suggests the crustal thinning of the oceanic basin, and the thickening of the continental boundary implies the opening of the SCS, which is connected and happened at the same time as the northern subduction of the proto-SCS. The Gravity modelling also suggests a large rifting event within the lithosphere that favors mantle upwelling.

1. Introduction

South China Sea (SCS) is a wedge-shaped marginal sea with a large oceanic crust in the east and a smaller amount in the southwest (Hsu et al., 2004). Sinistral strike-slip faults associated with the India-Asia collision were responsible for the formation of the SCS oceanic crust (Tapponnier et al., 1986) or Proto-South China Sea (PSCS) subduction underneath Palawan and northern Borneo (Sibuet et al., 2016; Hall, 2002; Lee and Lawver, 1995; Taylor and Hayes, 1983), or amalgamation of two processes (Morley, 2002). Investigating the development and distribution of SCS crust can reveal vital details about the SCS's tectonic evolution.

Tectonic interpretations of mantle structures beneath East Asia are non-unique and disputed, notably slab-like tomographic anomalies not associated with seismicity of the Benioff zone, despite general agreement about the long-term subduction history (Jin and Park, 2006). The north slab of the proto-SCS is the sub-horizontal, slab-kind deviations reaching 450–700 km depths directly beneath the SCS (Wu and Suppe, 2018). It has been argued that the ocean basin of the proto-SCS prevailed south of Eurasia, South China's mainland edge, before the current SCS (e.g., Taylor and Hayes, 1983; Holloway, 1982). On the other hand, the location of the subducted lithosphere of PSCS is a point of contention (Wu et al., 2016; Hall and Spakman, 2015; Zahirovic et al., 2014; Hall, 2002). Furthermore, it is questioned whether a proto-SCS existed (Replumaz and Tapponnier, 2003). To explain the evolution of SCS, proto-SCS, rifting, and magmatism, several geodynamic models have been developed from various geophysical methods (Li et al., 2021; Gozzard et al., 2019; Larsen et al., 2018; Sibuet et al., 2016; Lester et al.,

* Corresponding author.
E-mail address: satyageo41@gmail.com (A.V. Satyakumar).

https://doi.org/10.1016/j.pepi.2023.107107
Received 5 June 2023; Received in revised form 19 September 2023; Accepted 25 September 2023
Available online 26 September 2023

2014; Zhang and Wang, 2007; Braitenberg et al., 2006). These models suggested (1) the pre-rift crust in the western part of the SCS margin may be the reason that rifting was concentrated on narrow rifts and thinning focused on necking domains, (2) a major rifting event within the thin lithosphere permitted mantle upwelling resulted in a narrow and fast rift-to-drift transition along the northern SCS, (3) The opening of the whole SCS is linked and coincided with the northward subduction of the proto-SCS whose suture is located south of Palawan and extends westwards in north Borneo, and (4) seismic velocities are suggestive of highly thinned and magmatically intruded continental crust, the magmatic features are volcanic zones at the top of the basement that deforms or disrupt overlying post-rift strata, sills intruded into the post-rift sedimentary section, and a high-velocity lower crustal layer is the magmatic underplating or pervasive lower crustal intrusions. Several findings from the geological studies showed how rifting, the opening of SCS, upwelling of Hainan Plume, sedimentary infill, fault displacement, and thermal extension subsidence occurred at SCS (Yu et al., 2018a, 2018b; Sun et al., 2018; Jong and Barker, 2014; Mazur et al., 2012).

The young, moderately magmatic rifted margin of the South China Sea could provide vital new insights into the interaction of magmatism, rheology, and rifted margin structural evolution (Lester et al., 2014). Previous research discovered volcanic bodies strewn across the distal border, including a High-Velocity Lower Crust (HVLC) (Wang et al., 2006; Yan et al., 2001). This could be due to mafic underplating or widespread lower crustal intrusions. Throughout the SCS *syn*-rift and post-rift history, volcanic rocks have been recovered from boreholes in the continental shelf rift basins with diverse lithologies and ages (Lester et al., 2014; Yan et al., 2006). Despite signs of many syn-rift magmatic activities, no extensive observations have been made; therefore, the roles of magmatism and extension during rifting and continental breakup in the SCS are unknown. Grasp the SCS's ongoing tectonic and geodynamic processes requires a thorough understanding of its crustal structure. The nature of the crust throughout SCS has been more controversial. Hsu et al. (2004) assessed the northeastern SCS to have oceanic crust outboard the continental shelf edge rather than the extensive continental margin seen in other parts of the northern SCS margin based on magnetic evidence. Following gravity forward modelling, this crust was estimated to be 8–12 km thick (Yeh and Hsu, 2004), substantially thicker than ordinary ocean crust but possibly indicating thick oceanic or volcanic crust along magma-rich edges. However, recent seismic reflection studies in the northeastern SCS revealed skewed fault blocks indicative of substantially stretched continental crust (McIntosh et al., 2013; Lester and McIntosh, 2012). According to new magnetic modelling, magnetic anomalies regarded as weak lineations in ocean crust may instead suggest magmatically intruded continental crust (Yeh et al., 2012). In addition to these, many studies have examined the limitations of a basement, crustal structure, and the formation of distinct blocks in SCS (Li et al., 2021; Gozzard et al., 2019; Sibuet et al., 2016; Zhang and Wang, 2007; Braitenberg et al., 2006), however, there remain numerous outstanding problems regarding crustal architecture, state of isostasy, and how rifting and magmatic processes were influenced to formation and evolution of SCS. From investigations of bathymetry and Bouguer gravity anomalies, several continental uplifts, such as Reed Bank, Macclesfield Bank, Xisha Islands, Dangerous Grounds, and Zhongjian Massif, suggest a crustal heterogeneity (Chen et al., 2018). The impact of a diverse environment on rifting and the start of seafloor spreading requires investigating the diminished manner and magmatic state in SCS. When splitting the continent-ocean boundary, numerous criteria were employed to differentiate between the modified and actual oceanic crust coming from the mid-ocean ridge (MOR)s, and the extent of the sea province was estimated (Cameselle et al., 2017; Bai et al., 2014; Pichot et al., 2014; Barckhausen et al., 2014; Li et al., 2014; Wang et al., 2006; Nissen et al., 1995; Briais et al., 1993). Seismic and Magnetic investigations exhibit two periods of seafloor spreading in SCS (Ding et al., 2018; Li et al., 2014). The East Sub Basin (ESB) and the Northwest Sub Basin (NWSB) were formed first in the northern, then the expanding ridge moved to the southern, relinquishing the NWSB and establishing the Southwest Sub Basin (SWSB). Furthermore, conflicting outcomes were reported when detailing the typical crust beneath SWSB. Some mention it as the conventional crust of the SCS (Yu et al., 2017a, 2017b), and others refer to it as a serpentinized mantle below a thin and weakened crust (Yu et al., 2018a, 2018b). These conclusions point to significant disparities in magma supply and fluctuations driving the basin's expansion. We offer crustal structure from the recent high-resolution satellite gravity data and topography, geoid, and GyPSuM tomographic models to answer some of these problems.

With their global availability and fine resolution, satellite-based gravitational measurements are an excellent starting point for the wide-ranging research of the deep structure of the crust. The near-wavelength section of the gravity signal is often strongly associated with bathymetry over oceanic areas. The complete bathymetry model (Sandwell and Smith, 2001; Smith and Sandwell, 1997) incorporates global gravitational field anomaly and shipborne bathymetric estimates. Magnetic anomalies of the SCS basin were used to reconstruct the time of the breakup process beneath SCS, which was generated by sea-floor spreading and rifting (Briais et al., 1993; Taylor and Hayes, 1983). A magnetic anomaly was confirmed by the time of expansion on the shelf of SCS, located on the SCS's northern boundary (Clift and Lin, 2001; Bellingham and White, 2000; Su et al., 1989). Wang et al. (2001) and Hwang (1999) attributed by spreading axis in the SCS inferred from the gravity signal.

In this study, we decipher the Moho and isostatic compensation depth in the SCS and surrounding continental margins from the gravity and bathymetry datasets. In addition, geoid data and seismic tomography models were employed to better understand isostatic compensation and its emplacement, rifting, and magmatism processes. First, we estimated residual geoid anomalies at various degrees (10–50 degrees) and the computed Bouguer gravity anomalies, removing the sedimentary influence from the free-air gravity anomaly. The spectrum of the Bouguer gravity anomaly suggested transition wavelength revealed depths of the regional to local sources. The effective elastic thickness was estimated by measuring the crustal densities and topographies. We also measured Airy, flexural Moho from gravity Moho and effective elastic thickness and estimated inverted gravity Moho of various density differences. Furthermore, Bouguer gravity, geoid, and topography are used to calculate isostatic gravity anomalies and Geoid-Topography Ratio (GTR) values. Finally, 2D gravity modelling is used to comprehend the crustal architecture better, and the geodynamic implications are examined concerning previous models, magnetic directions, post-spreading volcanism, recent extension, seafloor spreading trends, and kinematic flow lines.

2. Tectonic background

In the west of the Pacific Ocean, SCS is a primary sea with continental boundaries formed due to tectonic cycles of Tethyan and paleo-Pacific (Zhou et al., 2008). The creation of SCS is caused by small continental chunks rifting on mainland Asia in the south, breaking from the extinct subduction zone over Palawan and the northern basin (Taylor and Hayes, 1983; Holloway, 1982). Towards the east, as the cutting edge of the Philippine Sea plate, the Luzon arc-trench system borders the SCS, with its northernmost piece overriding the SCS margin in the Taiwan portion. Currently, four major tectonic features surround SCS: the broken passive margin at the north, the subduction zone towards the east, the impacted thrust zone at the south, and the west-facing strike-slip fault region (Fig. 1A). Tectonically, SCS is bounded by the Indo-China terrane to the west, the Philippines oceanic plate towards the east, and the Yangtze plate in the north, with the subduction border connecting the Philippines oceanic plate and the Asian plate. From the early Cenozoic through Late Miocene, numerous tectonic events occurred at the SCS, and all of the plates surrounding the basin were

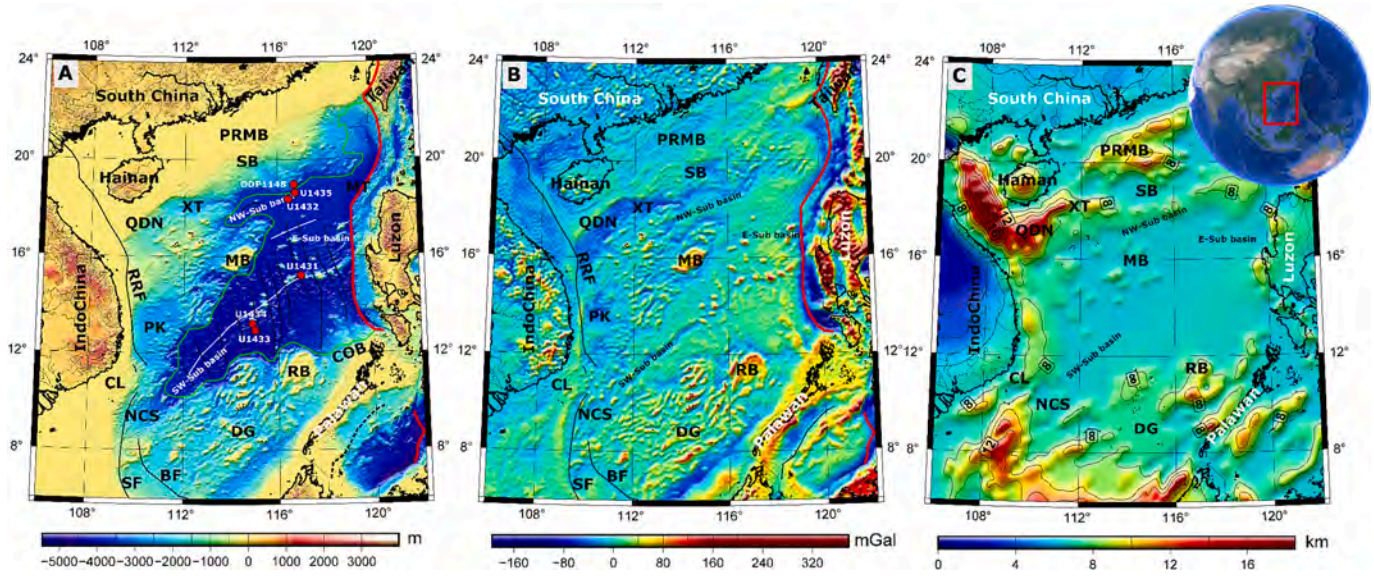

Fig. 1. (A) Bathymetry/Topography of South China Sea, superposed by tectonic features. Solid green line represents the continent-ocean boundary (COB), taken from Briais et al. (1993). Black solid lines are inactive transform faults. A thick red line is the active subduction zone. A solid white line indicates inactive spreading ridge, and a dotted black line represents the inactive subduction zone. Abbreviations:XT, Xisha Trough; SB, Shuangfeng Basin; PRMB, Pearl River Mouth Basin;MB, Macclesfield bank; RB, Reed Bank; DG, Dangerous Grounds; NCS, Nam Con Son basin; MT, Manila Trench; CL, Cuu Long basin; QDN, Qiongdongnan basin; PK, Phi Khan Basin; ESB, East Sub Basin (B) Free-air gravity anomaly map with major faults and ridges. (C) Sediment thickness map taken from National Centers for Environmental Information (NCEI; Whittaker et al., 2013).

rotated in a clockwise direction, subducted, and extruded (Yu et al., 2018a, 2018b; Barckhausen et al., 2014; Barckhausen and Roeser, 2004). There are four tectonic evolutionary stages in the SCS: (1) Rift structure growth, (2) Seafloor spreading, (3) SCS sinking, and (4) Taiwan uplift (Fyhn et al., 2009; Thies et al., 2005; Hall, 2002).

In the late Cretaceous to early Palaeocene, continental lithospheric rifting and thinning began with the primary uplift of rift bears and extensive erosion before the breakup of continents and beginning of seafloor spreading (Schlüter et al., 1996; Pigott and Ru, 1994). According to fault research at Pearl River Mouth Basin (PRMB) rift, at the minimum, two rifting events occurred at the SCS's north along the northern compound border (Pigott and Ru, 1994). NE-SW-oriented extensional faults originated from the previous Cretaceous-Palaeocene rift phase. E-W oriented normal faults characterize the second phase of late Eocene to early Oligocene rifting. After seafloor spreading ceased, district volcanic movement remains linked to another rifting event in the Middle Miocene (Zhao et al., 2016; Pigott and Ru, 1994). The Reed Bank, southern SCS margin, was active during the Paleogene, remained connected to a continent portion of South China, and most probably combined Northwest of Palawan, detached from Asia continent with the opening of South China Sea (Hutchison and Vijayan, 2010; Kudrass et al., 1985).

Data from International Ocean Discovery Program (IODP) expeditions (locations shown in Fig. 1A) constrain the nature of crust, petro-geochemistry type of basement, and seafloor spreading timeline (Jian et al., 2018; Sun et al., 2018; Li et al., 2015). Li et al. (2014) explained that the opening of the East Sub Basin (ESB) and the North-west Sub Basin (NWSB) had started around 33 Ma. At 25.5 Ma, the opening of the NWSB ended. Then, the ridge jumps happened at about 23.6 Ma and 27 Ma (Ding et al., 2018), and the spreading axis moved southward. The spreading halted at 15–16 Ma (Li et al., 2014); the most controversial issue is the SCS's enlarged activity, including deformational properties, the rifting process, and the breakup pattern. Indochina's extrusion force induced by the impact of India and Asia continents (Tapponnier et al., 1982) or tow force connected to proto-South China Sea south-eastward subduction near Borneo are still discussed possible driving mechanisms of seafloor spreading and rifting at South China Sea (Hall, 2002). Furthermore, the Hainan mantle plume may have aided in opening the South China Sea basin (Zhang et al., 2018), and it may likewise show a part in post-rift and synmagmatism at the South China Sea (Yan et al., 2014).

3. Data

Bathymetry map (Fig. 1A) is prepared based on GEBCO's global terrain model (GEBCO_2021), providing elevation data on a 15-s arc-space grid. The elevations range from −5500 to 3800 m; lower values are observed at the rifting center of the ocean basin, and higher values are found at the continental boundary. Briais et al. (1993) defined the Continent and Ocean boundary (green colour in Fig. 1A) as being usually bathymetry values depths of 2500–3000 m, with the northern segment being significantly deeper and terminating at the Manila Trench (MT).

The free air gravity anomaly map (Fig. 1B) is prepared on a $1' \times 1'$ marine gravity model (Sandwell et al., 2014), a vast improvement over the previous model. Jason-1 &Cryosat-2 were combined with existing data to obtain the thick volume with higher resolution in the ocean (Sandwell et al., 2014). High gravity anomalies are present in the Seamounts, carbonate platforms (MB & RB), Palawan, Luzon, and Taiwan; in contrast, low gravity anomalies are observed in the southwestern basin's mid-oceanic ridge and Palawan trough (Fig. 1B). The sediment thickness map (Fig. 1C) was created using a worldwide grid from the National Centers for Environmental Information (NCEI; Whittaker et al., 2013).

Because geoid anomalies are usually sensitive to deep density variations beneath the Earth, they shed light on the mechanisms that contribute to the formation of geological structures. The geoid map (Fig. 2A) is based on the Earth Gravitational Model EGM2008, representing 2159 degree and order of spherical harmonics (Pavlis et al., 2012). The geoid values range from −28 to 67 m; highs are found in Palawan and Luzon regions (SE part of study region), lows are observed in Indochina, Hainan, and South China areas (NW part of study region), and SCS basin showing intermediate values. The black rectangle boxes shown in Fig. 2A are the selected regions for the Geoid-Topography Ratio analysis to understand the compensation mechanism. To further know the mass deviations beneath the SCS, we created residual anomaly maps for different degrees of 10, 20, 30, 40, and 50, as shown in Figs. 2B,

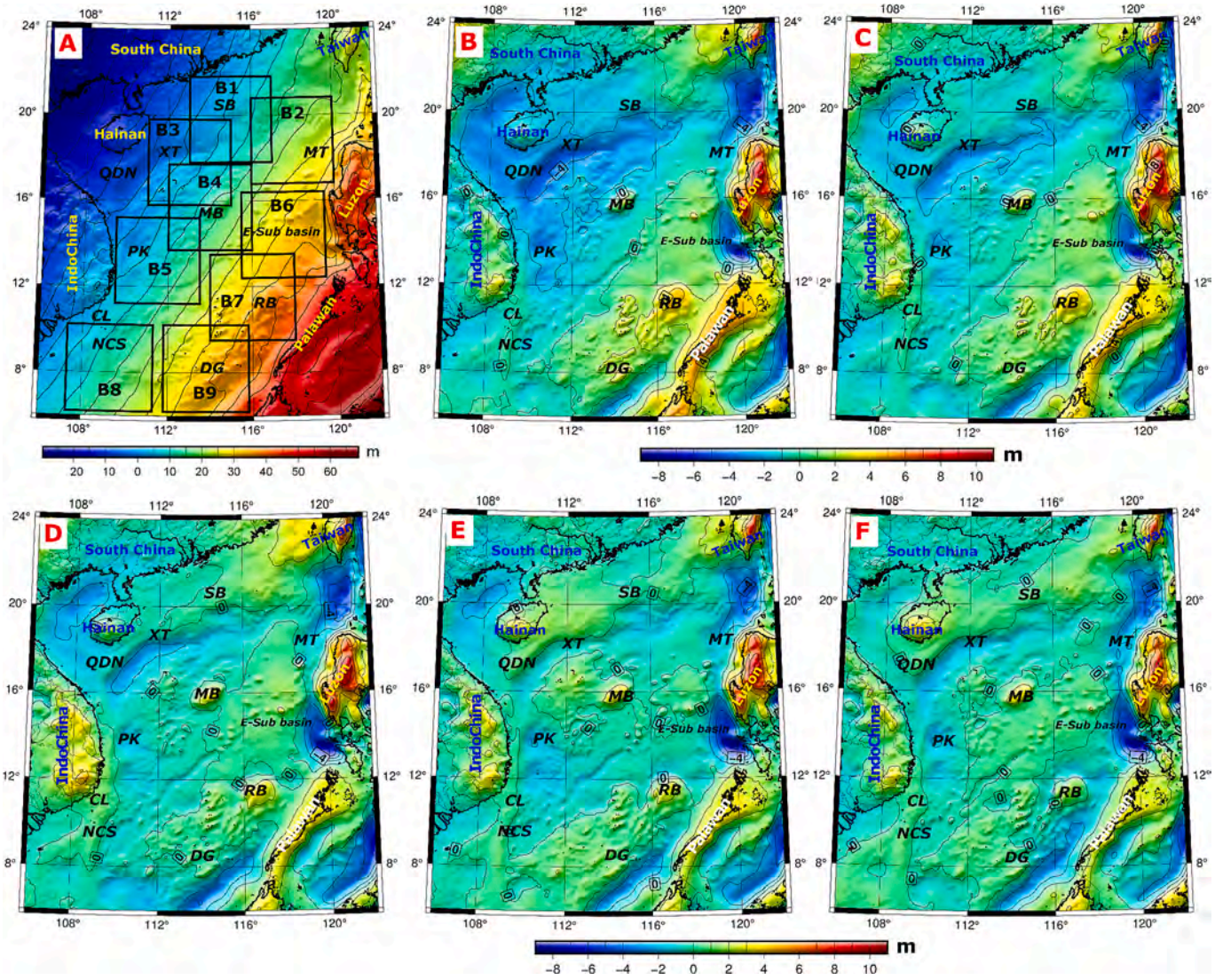

Fig. 2. (A) Geoid heights in South China Sea from the EGM2008 model (Pavlis et al., 2012). The selected blocks for the GTR analysis are outlined in the black boxes. Residual geoid maps of (B) degree-10, (C) degree-20, (D) degree-30, (E) degree-40, and (F) degree-50 were found afterward, eliminating long-wavelength influences from geoid (see text for details). Abbreviations are as in Fig. 1A.

C, D, E, and F, respectively, by subtracting the long-wavelength influences from original geoid displayed in Fig. 2A (Featherstone, 1997; Bowin, 1983). The residual geoid anomaly of degree-50 (~ < 800 km wavelength) is used to analyze the GTR variations, which represent the mass anomalies at a lower portion of the crust and top of the mantle (Featherstone, 1997; Bowin, 1983).

The free-air gravity anomalies are mostly subjective to the gravitational pull of bathymetry/sediments and their isostatic features. Therefore, a Complete Bouguer Gravity Anomaly (CBGA) is prepared by eliminating the impact of the water and sediments from free-air gravity anomalies. The terrain correction is applied based on surface height measurements for a better view of the ongoing processes of SCS and its deep crustal structure. Bouguer reduction density of 2.70 g/cm^3 and average crust thickness (30 km) is used for the Bouguer slab correction. The terrain/topography correction is applied based on the region's average crustal density of 2.70 g/cm^3, as our study area is mixed with land and ocean. Wang et al. (2000) provided the grain density of the South China Sea based on the ODP drilling results is about 2.70–2.80 g/cm^3; therefore, we used the topographic correction density as 2.70 g/cm^3. The topography effect on gravity anomaly is shown in Fig. S1C. The sediment effect is removed from the CBGA using the sediment thickness values (Fig. 1C), prepared sediment corrected Bouguer Gravity anomaly map (Fig. 3A). The sediment effect on gravity is calculated using the variable density contrast. The Quadratic function fitting formula for South China Sea calculates the density contrast based on the Depth and density variations relation (Yu et al., 2017a, 2017b). The density contract from the Quadratic function fitting formula for above 3 km is

$$\Delta\rho = -0.4076 + 0.0626^{*}Z - 0.0029^{*}Z^{*}Z$$

Here, Z is the sediment thickness in km.

The calculated density contrast for calculating the sediment effect on gravity of the South China Sea is shown in Fig. S1A. Using this density contrast, we calculated the sediment effect from the Parker algorithm. The sediment effect on gravity anomaly is shown in Fig. S1B. The Bouguer gravity anomalies range from −92 to 330 mGal, with highs observed at the SCS basin while lows found at continental margins. Hence, the SCS basin clearly shows the effect of the high density anomalies in the crustal part. Significant positive Bouguer anomalies in the central part of SCS indicate accreted dense material, uplifted and subsidized crustal basement.

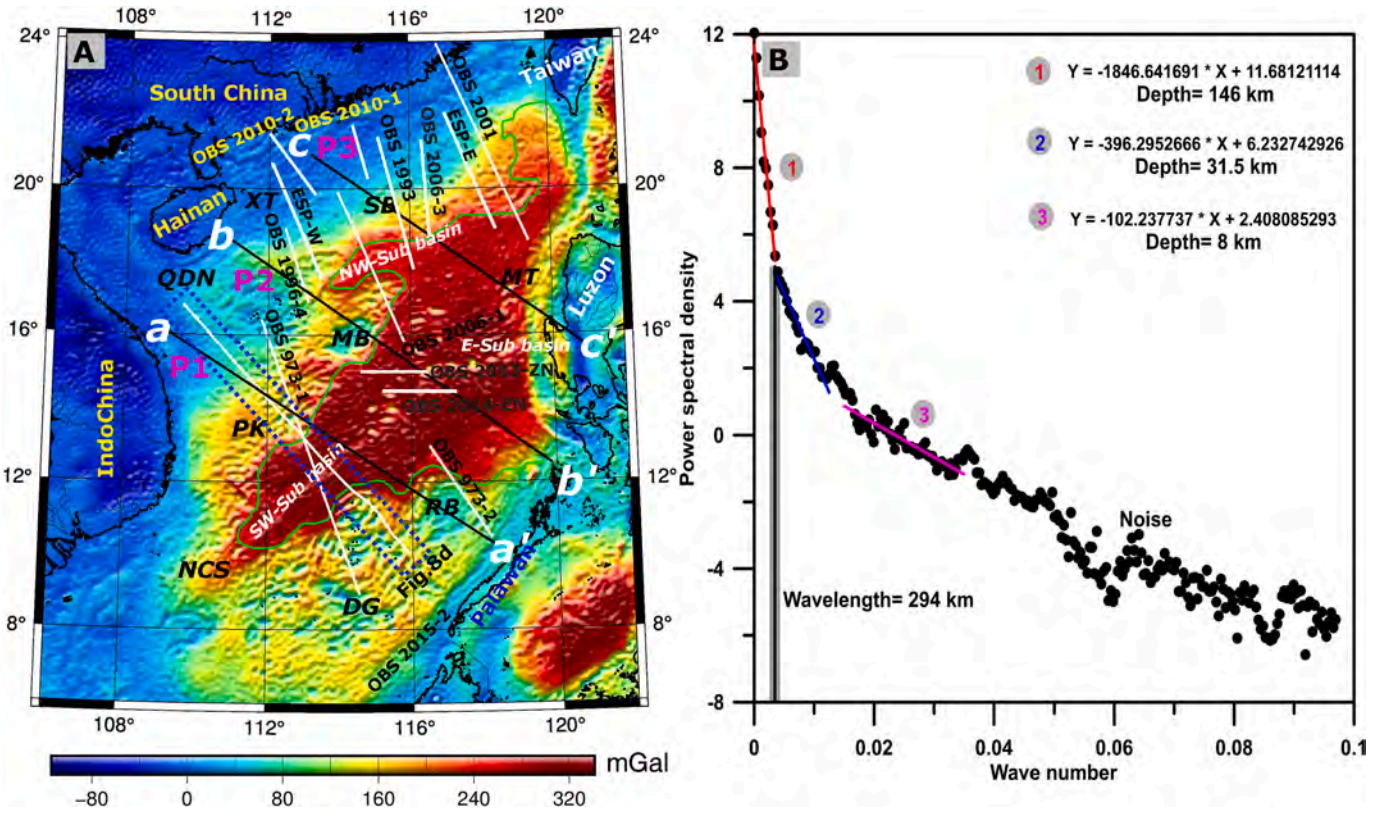

Fig. 3. (A) Complete Bouguer gravity anomaly map after subtracting the effects of the water column, sediment layer, and terrain correction applied based on surface measurements. The white lines are the seismic profiles in this region. The black lines are selected profiles for gravity modelling, indicating P1, P2, and P3. Abbreviations are as in Fig. 1A. (B) Power spectral density (PSD) versus wavenumber of Bouguer gravity anomaly. Three average depths of 146 km, 31.5 km, and 8 km have been obtained from the association between PSD and Wave No.

4. Methodology

4.1. Power spectrum of Bouguer gravity anomaly

Spectrum of gravity anomaly is frequently used as first-hand evidence of depth to causative sources (Mishra and Pederson, 1982) and yields estimates of apparent depth to sources. The radially averaged power spectrum of Bouguer gravity anomalies is computed, and the slope is estimated from the least-square fit of the power spectrum. Further depth (h) of a successive anomalous layer is calculated by dividing the slope of each straight line by 4Π. h = P(k_1)-P(k_2)/4Π (k_1−k_2); here, k_1 and k_2 are the start and end points of radial frequencies, and P(k_1), P(k_2) are the corresponding values of radially averaged power spectrum component (Spector and Grant, 1970; Guo et al., 2013).

The power spectrum of Bouguer gravity anomalies will provide source depths and the wavelength for separating regional and residual anomalies. In this study, we used the power spectrum method to calculate the depth of the sources. The radial spectrum of the Bouguer anomaly of the study region (Fig. 3B) mainly shows three slopes attributed to causative sources at a depth of 146 km, 31.5 km, and 8 km. The power spectrum is an important tool for knowing the source depth of Moho. The computed source depths suggest lithospheric, continental, and oceanic crust depths of 146, 31.5, and 8 km. The depth of 31.5 km is used as a reference level for determining Moho in gravity inversion, which consistent with previous studies (e.g., Nissen et al., 1995; Yan et al., 2001; Wang et al., 2006; Franke et al., 2011; McIntosh et al., 2014; Pichot et al., 2014). The study region contains several tectonic domains in which Moho depths vary significantly; therefore, validating the calculated reference level from the power spectrum for the entire area is very important. In this manner, we calculated the power spectrum of each subset (locations in Fig. 2A) and found that the average Moho depth is about ~31 km (Fig. S7).

4.2. Gravity Moho from Parker-Oldenburg inversion

The Parker-Oldenburg (Oldenburg, 1974) iterative approach for inverting density interfaces from gravity anomalies has been frequently employed in potential fields. Predicting the crust-mantle interface from the inverse problem gave a preset contrast of density that could be used to determine the topographic Moho variations via gravity anomaly. In the Fourier transform, proposed by Parker (1973), the gravitational anomaly, g, is related to variations in boundary, h(x), about the depth of the reference plane, z_0

$$F(\Delta g) = 2\pi G\Delta\rho e^{(-kz_0)}\sum_{n=0}^{\infty}\frac{K^{n-1}}{n!}F[h^n(x)] \quad (1)$$

F (Δg), Fourier domain of gravitational field, G denotes the universal gravitation constant, Δρ signifies the density difference between crust-mantle boundary, and finally, k indicates the modified vector wave function.

The rearrangement of the above equation by Oldenburg (1974) as an iterative algorithm:

$$F[h(x)] = -\frac{F[\Delta g(x)]e^{(-kz_0)}}{2\pi G\Delta\rho} - \sum_{n=2}^{\infty}\frac{k^{n-1}}{n!}F[h^n(x)] \quad (2)$$

Moho depth from the gravitational field (Zcg) is found below:

$$Zcg = z_0 + h(x) \quad (3)$$

To the iterative process convergence of Eq. (2), Oldenburg (1974) restricted a filter.

$$A(k) = \frac{1}{2}\left[1 + cos\left(\frac{k - 2\pi K_L}{2(K_H - K_L)}\right)\right] \text{ for } K_L < k < K_H \quad (4)$$

where

$A(k) = 0$ for $k > K_H$.

$A(k) = 1$ for $k < K_L$.

The filter A (k) dampens high frequency observations.

So, it is possible to calculate Moho depth h(x) as a function of the average depth by Eq. (2) repetitively using reference level, z_0, density disparity between crust and mantle, and transitional frequencies (K_H & K_L), and then derive the gravity Moho depth, Z_{cg}, using Eq. (3). We used the single layer inversion based on spectral analysis with a density of 0.4 to 0.6 g/cm^3 and a reference depth of 31.5 km. The present study area covers the continental and ocean parts; the crust and mantle densities of continents and oceans vary significantly. For example, the crustal density of continents is about ~2.70 g/cm^3. The ocean basin varies from 2.8 to 2.90 g/cm^3, and mantle density varies ~3.20–3.30 g/cm^3. These average values are taken from the previously published multi-channel seismic and OBS data (e.g., Nissen et al., 1995; Yan et al., 2001; Wang et al., 2006; Franke et al., 2011; Lester et al., 2013; McIntosh et al., 2014; Pichot et al., 2014; Ruan et al., 2016; Zhao et al., 2018; Huang et al., 2019). Therefore, we used density contrasts of 0.4 to 0.6 g/cm^3 for gravity inversion.

4.3. Isostatic Moho from airy and flexural models

We used the local (Airy) and regional (Flexural) models described below to calculate the isostatic Moho. At the compensation level, the Airy model is known as a local isostatic compensation model, in which each column exerts equal pressure. The flexural (Vening Meinesz) model depicts regional compensation by imagining a light upper layer that floats on a denser fluid and acts as an elastic plate overlying a weak fluid. The flexural model depends on the elastic properties of the lithosphere.

4.3.1. Airy model

The compensation required by isostasy can be achieved using the Airy based model. The decreasing crust-mantle interface is attributed to excess topography mass filling (Wang et al., 2003; Watts, 2001). According to the Airy model, the elevations are closely related to Moho depth, and the compensation percentage significantly impacts the geologic context (Wang et al., 2009a, 2009b). Therefore, concerning Airy isostatic model

$$\rho_c(H + t) = \rho_m t \quad (5)$$

$$t = \left(\frac{\rho_c}{\rho_m - \rho_c}\right)H \quad (6)$$

Finally, the Airy-based crust-mantle interface $Z = Z_0 + t$, where Z_0, standard isostatic Moho (in km), t refers to the root (in km), H denotes the topography, ρ_c, and ρ_m represent crustal and mantle densities. More details about root (t) calculation using topography (H) are discussed in Section 5.2.1.

4.3.2. Flexural model

In the regional isostasy model, compensatory mass loads are dispersed entirely within the crust. As a result, compensation is performed by changing the thickness or depth of the Moho interface. Indeed, the elasticity of rocks deforms a flexible crust, which sustains near-wavelength topography mass that generates a flexure nature. On the other hand, significant changes in Moho variations are caused by long-wavelength surface displacements and ductile flow in the heated lower crust. Excess load of topographic features deflects the Moho contact downward a distance w. The Moho interface can be deflected by two parameters: Effective Elastic Thickness (T_e) and flexural rigidity. Nadai and Hodge (1963) explain flexural hook (w) at point coordinate as follows:

$$D\nabla^4 w(x) + g(\rho_m - \rho_c)w(x) = L(x) \quad (7)$$

Here, L is the topographic load, g refers to acceleration due to gravity, D refers to flexural rigidity, and $D = E \times T_e^3/[12(1 - \sigma^2)]$. Poisson ratio and Young's modulus are σ and E, respectively. Table S1 shows the parameters used to determine the flexural responses.

At the point of load, Hertz (1895) discussed the precise answer to Eq. (7), which is written in Bessel-Kelvin representations (Abd-Elmotaal, 1993; Gruninger, 1990). Instead, VeningMeinesz (1940) proposed a strategy using the degree of regionality and maximum deflection.

$$w_0 = \frac{m_L}{8(\rho_m - \rho_c)l^2} \quad (8)$$

where m_L stands for load mass-created through the topography, l stands for the degree of regionality, and w_0 denotes the maximum deflection (VeningMeinesz, 1940)

$$l = \sqrt[4]{\frac{D}{g(\rho_m - \rho_c)}} \quad (9)$$

In all practical applications, the discrepancy between the exact and approximate solutions can be ignored (Abd-Elmotaal, 1993, 1995; Gruninger, 1990). To achieve an approximate solution to Eq. (7), a modest approach was created using the Moho variations at a distance (r) from the load (VeningMeinesz, 1940). The following are the polynomial equations and their solutions:

$$\frac{w_1}{w_0} = c_1\left(\frac{r}{l}\right)^6 + c_2\left(\frac{r}{l}\right)^4 + c_3\left(\frac{r}{l}\right)^2 + c_4 \; 0 < \frac{r}{l} < 2 \quad (10)$$

$$\frac{w_2}{w_0} = c_5\left(\frac{r}{l}\right)^4 + c_6\left(\frac{r}{l}\right)^2 + c_7 \; 0 < \frac{r}{l} < r_{max} \quad (11)$$

Here, r_{max}, the curvature radius at compensation depth, can be written as r_{max}=l*2.905 (VeningMeinesz, 1940). As a result, Eqs. (10) and (11) are used to estimate the vertical deflections of the bending as follows,

$$w = w_1 + w_2 \quad (12)$$

The mass of load m_L owing to the topographic density (ρ_c), elevation (h), and area (ds) for computing the Vening-Meinesz compensatory depths can be represented as:

$$m_L = \rho_c h ds \quad (13)$$

As a result, the bending caused by the topography (Moritz, 1990) with mass load is

$$Zm_L = w(r)\rho_c h \, ds \quad (14)$$

Here, Z is the average crustal thickness, Bending due to the full masses (Abd-Elmotaal, 1995; Moritz, 1990):

$$w(x) = \iint \rho_c h(x')w(r)ds \quad (15)$$

The overall bending is thoroughly connected to the depth of Moho,

$$h_M = T_0 + w \quad (16)$$

Here, T_0 is the thickness of the crust aimed at topography concerning sea level.

4.4. 2D modelling of gravity anomaly

We carried out 2D modelling of gravity anomaly through the selected profiles to further support sub surface architecture and density fluctuations beneath the SCS basin (locations shown in Fig. 3A). We studied the gravity fields to attain a reasonable density structure; as it is widely known, the modelling of gravity fields unaided is not unique. Separating mass inhomogeneities within the mantle from those restricted to the

crust will be easier with the combined usage of gravity undulations. The crust, lithospheric thickness, and density values affect gravity anomalies and topography. As a result, distance to the source and gravity variations are affected, while elevation is unaffected by distance; all are effective throughout a wide range of depths (Zeyen and Fernàndez, 1994). Therefore, we removed the deeper lithospheric effect on the Bouguer gravity anomaly and calculated the Residual Bouguer anomalies (RBA) used for the modelling. RBA is computed using the high pass filter of 294 km wavelength (Power spectrum, Fig. 3B) from the Bouguer gravity anomaly. GMSYS-2000 software (GMSYS, 2000) calculates gravity anomalies using 2D Talwani's algorithm (Talwani et al., 1959). The initial geometry of Moho is attained from the inverted crustal structure from gravity data. The Moho's geometry is tweaked until the optimum fit is found. Finally, we included crustal density sources in the modeled section based on documented geology and geophysical cross-sections to match the short-wavelength anomalies. Densities of 2.70, 2.90, and 3.30 g/cm^3 were aimed at the continental crust (upper & lower) and lithospheric mantle. The top and lower oceanic crusts have a density of 2.80 and 3.00 g/cm^3, respectively. The density constraints are the average values of previously published multi-channel seismic and OBS data (e.g., Nissen et al., 1995; Yan et al., 2001; Wang et al., 2006; Franke et al., 2011; Lester et al., 2013; McIntosh et al., 2014; Pichot et al., 2014;

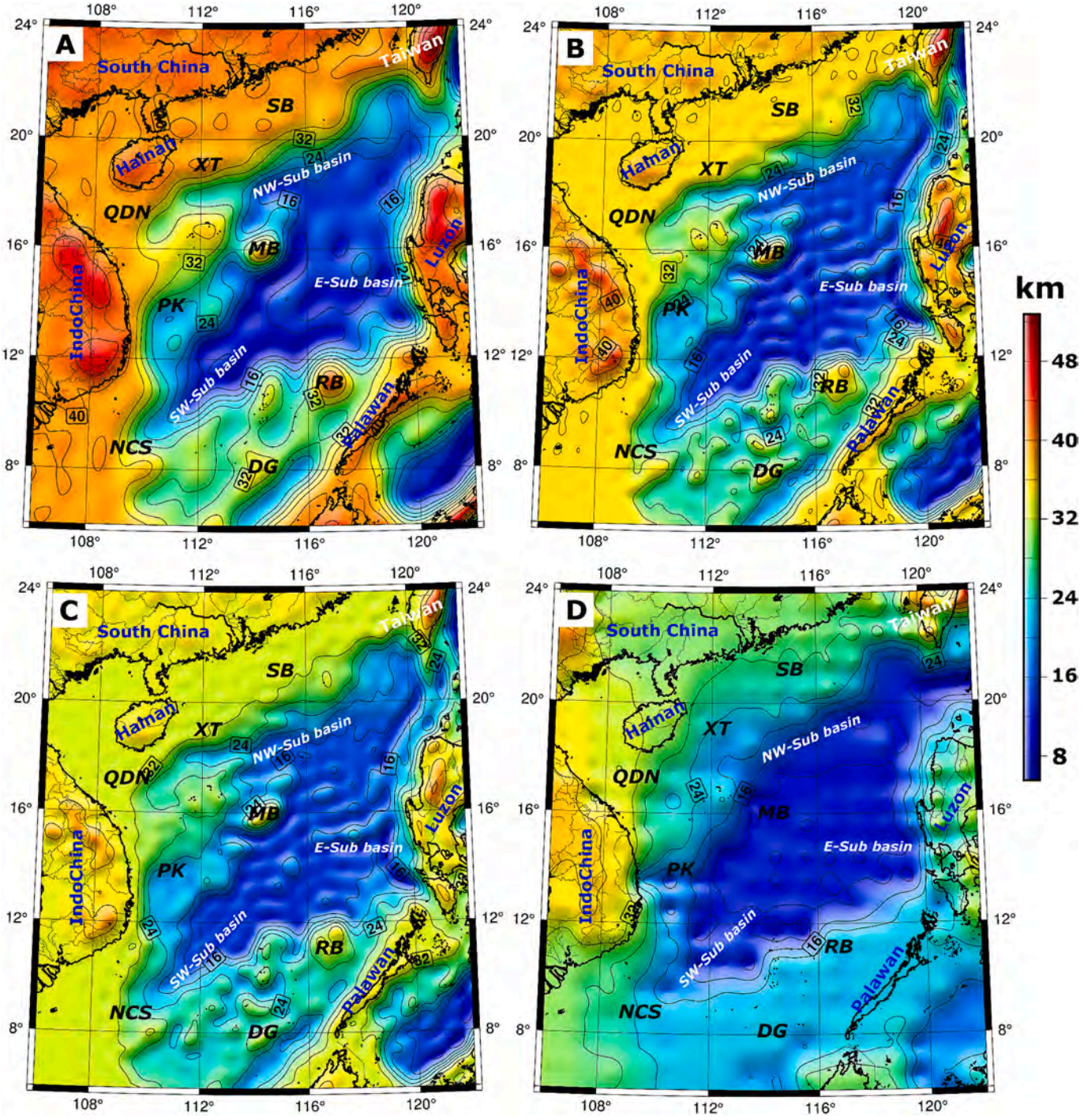

Fig. 4. Moho depth from inversion of gravity data (A) density contrast of 0.4 g/cm^3 (B) density contrast of 0.5 g/cm^3 (C) density contrast of 0.6 g/cm^3 (D) CRUST1.0 model (Laske et al., 2013). Abbreviations are as in Fig. 1A.

Ruan et al., 2016; Zhao et al., 2018; Huang et al., 2019).

5. Results and analysis

5.1. Gravity Moho

The Moho variations beneath the SCS and surrounding areas from gravity inversion using different density contrasts of 0.4, 0.5, and 0.6 g/cm^3 are presented in Figs. 4A, B, and C, respectively. These findings imply Moho varies between 7 and 48 km, with lower values beneath the SCS basin and greater in the Indochina continental region. The fluctuations in Moho were detected when the density contrast between the crust-mantle interface was changed between 0.4 and 0.6 g/cm^3. The Moho varies from 9 to 45 km (Fig. 4A), where 0.4 g/cm^3 was introduced. We utilized a 0.5 g/cm^3 contrast and found that Moho's result varies from 7 to 52 km (Fig. 4B). Finally, we used a 0.6 g/cm^3 contrast and found that the Moho fluctuations are 7–48 km (Fig. 4C). Places with a 7–8 km crust are interpreted as a crust of ocean area and an extended continental crust; nevertheless, some of these areas could cover a combination of mainland pieces and or exhumed mantle/mafic substance.

Gravity Moho is mostly close to the seismic Moho attained from CRUST1.0 (Fig. 4D), but some deviations could be a lower resolution of CRUST1.0. Our moho findings slightly vary with the former geophysical research investigations, but the average values are in good correlation (e.g., Li et al., 2021; Gozzard et al., 2019; Sibuet et al., 2016; Zhang and Wang, 2007; Braitenberg et al., 2006; Shi et al., 2000). However, all these studies do not have the same crustal architecture. The thinned continental crust suggests Moho depth, 10–12 km in the northern part, different from the southern part (8–10 km). The anticipated crustal thickness and Moho depth (Fig. 4) grow northwards of the South China mainland margin to 35 km. On the other hand, the depth of Moho and crust beneath the Dangerous Grounds are low, ranging from 10 to 30 and 15 to 30 km, respectively. Cuu Long (CL) and Nam Con Son (NCS) basins, off the coast of southern Vietnam, are projected to have thinner continental crust; the crust of NCS is expected to be between 13 and 18 km thick. This basin, considered Miocene in age, was generated before the seafloor spreading propagating tip. The wide-angle seismic profiles (OBS2013-ZN & OBS2014-ZN) show crust has a thickness of 5–8 km and Moho depth in the ocean basin of approximately 6–7 km with a low velocity of 7.6 km/s (Ruan et al., 2016), our Moho depths (Fig. 4A, B, C) shows 6.5 to 12 km. The Moho of 6–24 km was obtained from the OBS2014 seismic line (Pichot et al., 2014); our Moho models (Fig. 4A, B, C) show 7–30 km. OBS973–1 and OBS973–2 seismic profiles (Wei et al., 2011, 2015) show the moho varies from 5 to 24 km, and our Moho varies from 6.5 to 26 km. The seismic studies (OBS1996–4 (Qiu et al., 2001), ESP—W, E (Nissen et al., 1995), OBS2010–1 and OBS2010–2 (Cao et al., 2014 and Zhu et al., 2017)) showed the Moho varies 15–28 km, our gravity Moho varies 18–32 km. The other seismic surveys (OBS1993 (Yan et al., 2001), OBS2006–3 (Qiu et al., 2011), OBS2001 (Wang et al., 2006), OBS2006–1 (Wu et al., 2011)) show the Moho varying 6–25 km, our Moho models shows 8–29 km. We found the differences (uncertainties) between seismic Moho and our gravity inversion Moho at 4–7 km.

The South China block and Indochina coastal zone exhibit a Moho depth variation gradient, with a 6 km increase from 30 km in the South China block to 36 km in Indochina. This gravity Moho of 0.6 g/cm^3 contrast is compared through topography and the Bouguer gravity anomalies to assess the isostatic nature. The scatter plot of gravity Moho, topography, and Bouguer anomalies are prepared and shown in Figs. 5A and B. The linear relationship is observed in the gravity Moho and topography, whereas an inverse relation is found in the gravity Moho and Bouguer anomaly. This relationship between gravity Moho and topography is utilized to compute Airy isostatic Moho.

5.2. Isostatic Moho

In this paper, we reported the isostatic Moho from the Airy and flexural models; the results are in good agreement, and the following sections provide more information.

5.2.1. Airy-isostatic Moho

Using the least-squares linear regression, we can find the connection $z_{cg} = 32.8 + 0.004\times$ t by comparing the topography (t) and gravity Moho (z_{cg}) from Fig. 5A. The gravity Moho depth to the Moho from gravity inversion, 32.8 km, matches the zero-topography level.

The crustal density (ρ_c) of 2.70 g/cm^3 and mantle density (ρ_m) of 3.30 g/cm^3 was used. We computed $t = 4.5$*H, where H is topography in km (from Eq. 6). Because the depth of Moho (isostatic) da = T + t (T is

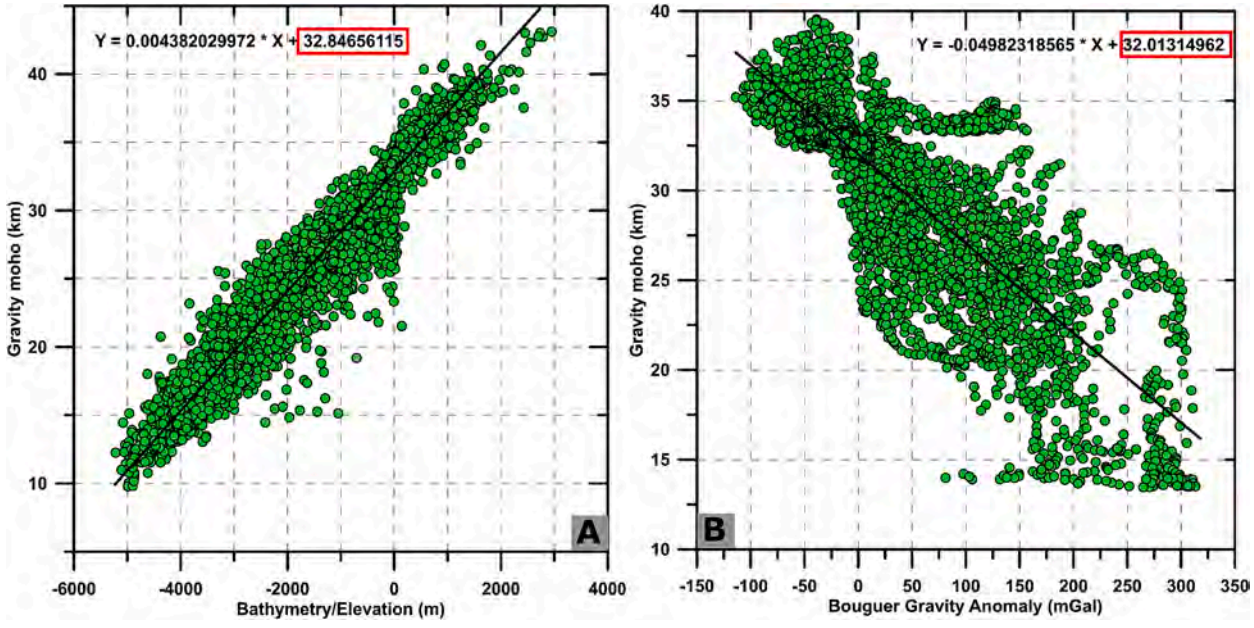

Fig. 5. Scatter plot between (A) Bathymetry/Topography versus Gravity Moho (B) Bouguer gravity versus Gravity Moho, with regression line (solid black line). Note that the regression line shows the standard isostatic Moho of ~32 km.

the average Moho (isostatic). T is root), we consider 32.8 km the standard isostatic Moho. $d_a = 32.8 + 4.5H$ yields the isostatic Moho in this case. The isostatic Moho from the Airy model ranges from 8 to 45 km (Fig. 6A). Our findings are in good correlation with the CRUST 1.0 model, ranging from 9 to 43 km. The gravity Moho and the Airy-isostatic Moho are mostly correlated to each other. If Moho from gravity inversion is higher than Moho from isostatic correction, the elevation/bathymetry will increase, producing higher elevations and a deeper Moho (isostatic) to maintain equilibrium.

5.2.2. Flexural isostatic Moho

The surface elevation data in Fig. 1A represents the topographic loads, and 0.6 g/cm^3 contrast is considered based on standard density values of the mantle, 3.30 g/cm^3, and crust, 2.70 g/cm^3. Rather than Effective Elastic Thickness (T_e), choosing T is essential in mapping Moho undulations. Even though T has no predictive value in this area, some research provides an approximation (Li et al., 2021; Gozzard et al., 2019; Sibuet et al., 2016; Zhang and Wang, 2007; Braitenberg et al., 2006; Shi et al., 2000). As a result, we used T as 31.5 km from the Bouguer gravity spectrum and the relationship between gravity Moho and topography when topography is practically zero (Figs. 3B, 5A). Using the Maximum Entropy Method, the T_e value of 16 km is computed from the coherence between topography and Bouguer anomaly (Lowry and Smith, 1994; Fig. S3). The computed Moho depths from Flexural isostatic compensation are presented in Fig. 6B). The Moho undulation features are smoothed under the middle section of SCS, which corresponds to lesser terrain, and its shape is generally smooth with a range of 7–41 km. On the other hand, the Moho undulations are noticeable on either side of SCS. The Indochina, South China main lands, and Luzon blocks have the greatest isostatic Moho deepening, while the middle region of the SCS has the smallest Moho depths (Fig. 6B). The places through major variation in isostatic Moho are underneath continental margins, resulting from many plates in continental areas, including the Philippine Sea, Southern South China Sea, and Eurasia. In general, higher altitudes in the region are thought to push down the crust and its surroundings due to depths in isostatic Moho.

Nevertheless, depressions in this area result in sedimentary basins, which operate like negative load, compensating for greater altitudes (positive load). The flexural distortion deeds, like the high-cut filter for horizontal dissemination of the loads, are shown in Fig. 6B. Topographic loads in the Indochina, South China, and Luzon blocks generate cavernous and spare depressions for distorted lithosphere; however, numerous basins or rigid lithosphere may cause wide and shallow depressions. Furthermore, the scatter plot between gravity Moho and isostatic Moho is prepared; it is worth mentioning that the isostatic Moho from both Airy and flexural models were highly correlated with gravity Moho with correlation coefficients of ~1 (Fig. 6C), with an error of ±3 km.

5.3. Apparent isostatic compensation depth

The Geoid to Topography Ratio (GTR) is an additional significant constraint for determining the compensation mechanism of volcanic features in oceanic areas (Sandwell and MacKenzie, 1989; Haxby and Turcotte, 1978). GTR was calculated along with the nine selected subsets within SCS (blocks shown in Fig. 2A). The residual geoid is acquired by deleting the long-wavelength section of degree and order 50 spherical harmonic expansion. The GTR is calculated using the gradient of the true-fitting reversion line of residual geoid-basement correlation. Following Monnereau and Cazenave's technique (Monnereau and Cazenave, 1988), the calculated GTR is transformed to apparent compensation depths (dc). Fig. 7 depicts the scatter plot between the residual geoid, residual basement, and the GTR vales produced. The GTR values obtained range from 0.55 to 1.41 m/km, with a greater value at block-8 (NCS) and a lower value at block-6 (ESB). Table 1 shows the Geoid-topography ratio and accompanying depth of compensation measurements for nine subsets. The ESB (block-6) and NCS (block-8) have shallow depths of compensation (11 km) and deeper depths of compensation (28 km), respectively. Small GTR measurements of 0–2.1 m/km designate narrow topographic compensation, while middle GTR outcomes (2–6.1 m/km) imply greater compensation depths owing to lithospheric thinning, according to Crough (1978). The high Geoid-topography ratio (> 6.1 m/km), on the other hand, shows sub-lithospheric correction (McKenzie et al., 1980). The shallow level of compensation found in SCS with our findings.

5.4. Constrained gravity modelling

The central SCS basin is characterized by high gravity and low topography. As a measure of crustal thinning, we found the amplitude and the size of the positive Bouguer anomalies seen in Fig. 3A. These could be attributable to a shallow/exposed crust and high-density material at the Moho level. The Bouguer gravity anomalies are a combined effect of crustal and lithosphere; our main objective is deciphering

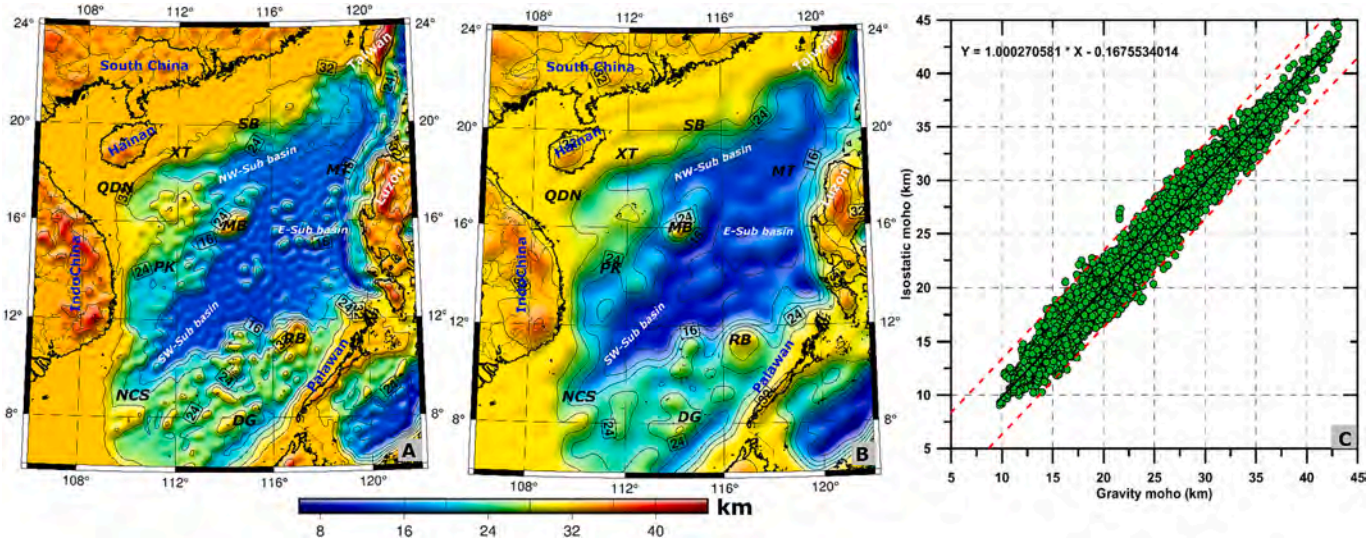

Fig. 6. The isostatic Moho (A) Airy model (B) Flexural model. Abbreviations are as in Fig. 1A. (C) Scatter plot among gravity and isostatic Moho shows a relationship coefficient of ~1.

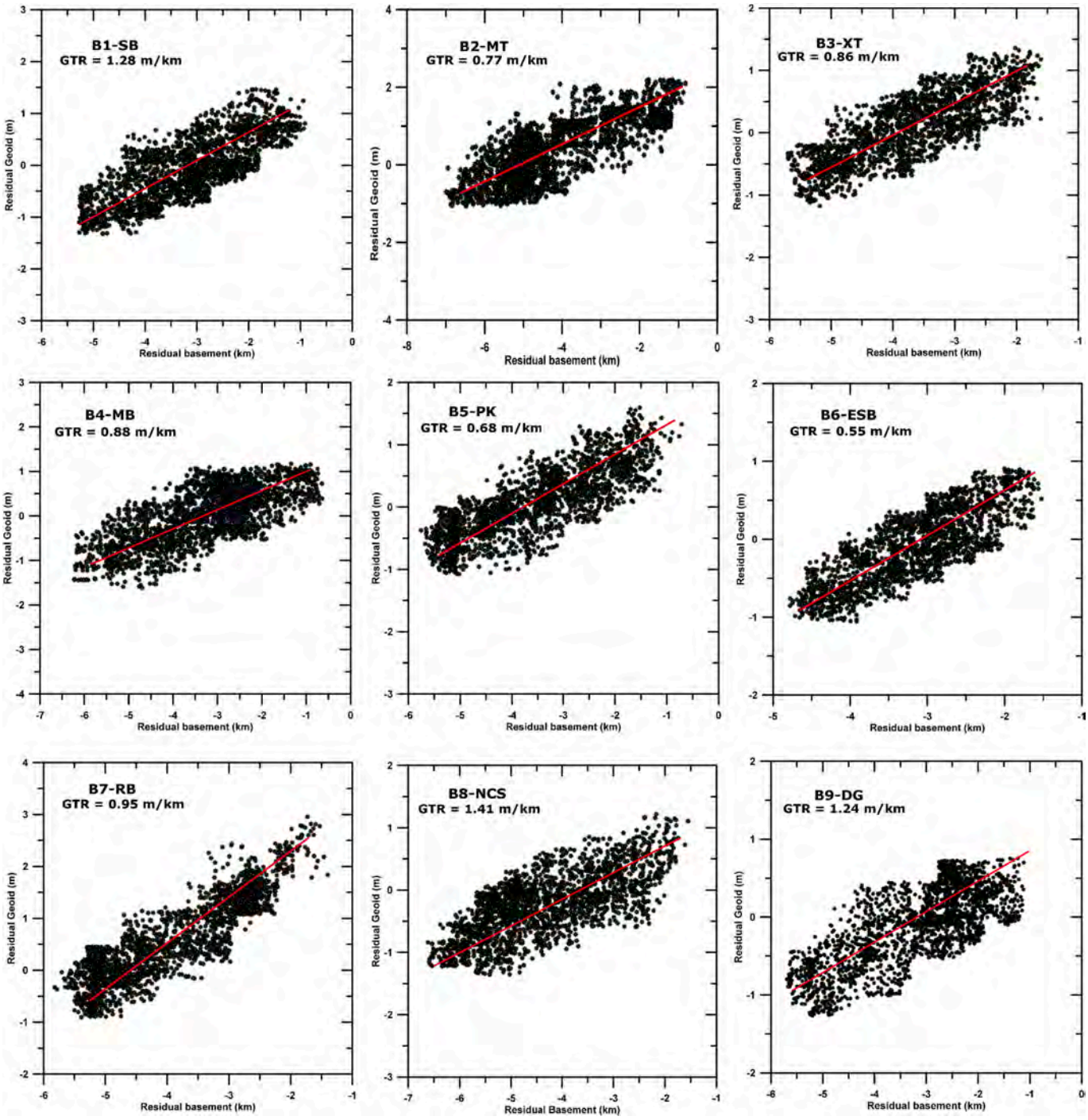

Fig. 7. Geoid to topography ratio (GTR) plots along with the selected blocks (block locations are in Fig. 2A). Red line represents the regression line to measure GTR value. (For interpretation of the references to colour in this figure legend, the reader is referred to the web version of this article.)

crustal structure. Therefore, we removed the lithospheric effect on Bouguer gravity anomalies and computed Residual Bouguer anomalies (RBA) for the modelling. The thin crust is due to an abnormally big mantle plug, while the thick crust has a higher topography. In the latest, a substantial amount of deep and multi-channel seismic surveys and associated investigations were conducted in the South China Sea (Qiu et al., 2012), providing us with constraints for gravity modelling. For gravity modelling, we chose three profiles crossing the RB, MB, and SB (in Fig. 3A). The computed crustal and mantle sections, along with their densities, are presented in Fig. 8, with mantle upliftment in the SCS basin's center and the usual Moho on each side.

5.4.1. Profile-1 (aa')

Profile-1 (Fig. 3A) runs for 1160 km in an NW–SE direction, passing mainly through the PhuKhanha basin, Southwest Sub-Basin, U1434, U1433, Reed Bank, and Palawan block. For shallow information, the NH973–1 profile of seismic (Ding et al., 2013; Li et al., 2010) was used, and for in-depth knowledge, the OBS973–1 profile of Qiu et al. (2011) was used. The modeled crustal structure divided into two sections: one beneath the Southwest Sub-Basin, and the other on either side of continental boundaries (Fig. 8A). The crust is thin, with a Moho depth of only 9–14 km in SWSB, suggesting the typical oceanic crustal structures. Cenozoic sediments range in thickness from 1 to 3 km. The continental

Table 1
Results of Geoid-Topography Ratio (GTR), Depth of compensation, Gravity Moho, and isostatic Moho, and Crust1.0 for the selected blocks (B1-B9).

Block Name	Center Point	GTR m/km	Depth of Compensation (km)	Gravity Moho (km)			Isostatic Moho (km)		Crust 1.0
				0.4 (DC)	0.5 (DC)	0.6 (DC)	Airy	Flexural	
B1-SB	115E, 19.8 N	1.28	26.0239	32.1	28.6	26.8	26.3	25.4	24.2
B2-MT	118E, 18.8 N	0.77	15.6550	15.5	16.2	16.4	15.6	13.7	14.6
B3-XT	113E, 17.8 N	0.86	17.4848	26.5	26.9	25.4	24.7	22.8	21.15
B4-MB	114E, 15.7 N	0.88	17.8914	34.1	36.6	33.4	33.5	29.4	28.11
B5-PK	111.5E, 13.2 N	0.68	13.8252	22.2	21.2	20.7	20.2	19.2	18.3
B6-ESB	117.5E, 11.5 N	0.55	11.1821	31.3	29.6	27.7	27.2	26.7	24.6
B7-RB	116E, 11.5 N	0.95	19.3146	24.3	24.6	23.5	23.1	21.1	19.8
B8-NCS	109.3E, 8.2 N	1.41	28.2106	35.8	32.7	30.2	29.5	27.9	26.8
B9-DG	113.8E, 8.2 N	1.24	25.2106	32.1	27.1	25.5	25.6	24.1	22.3

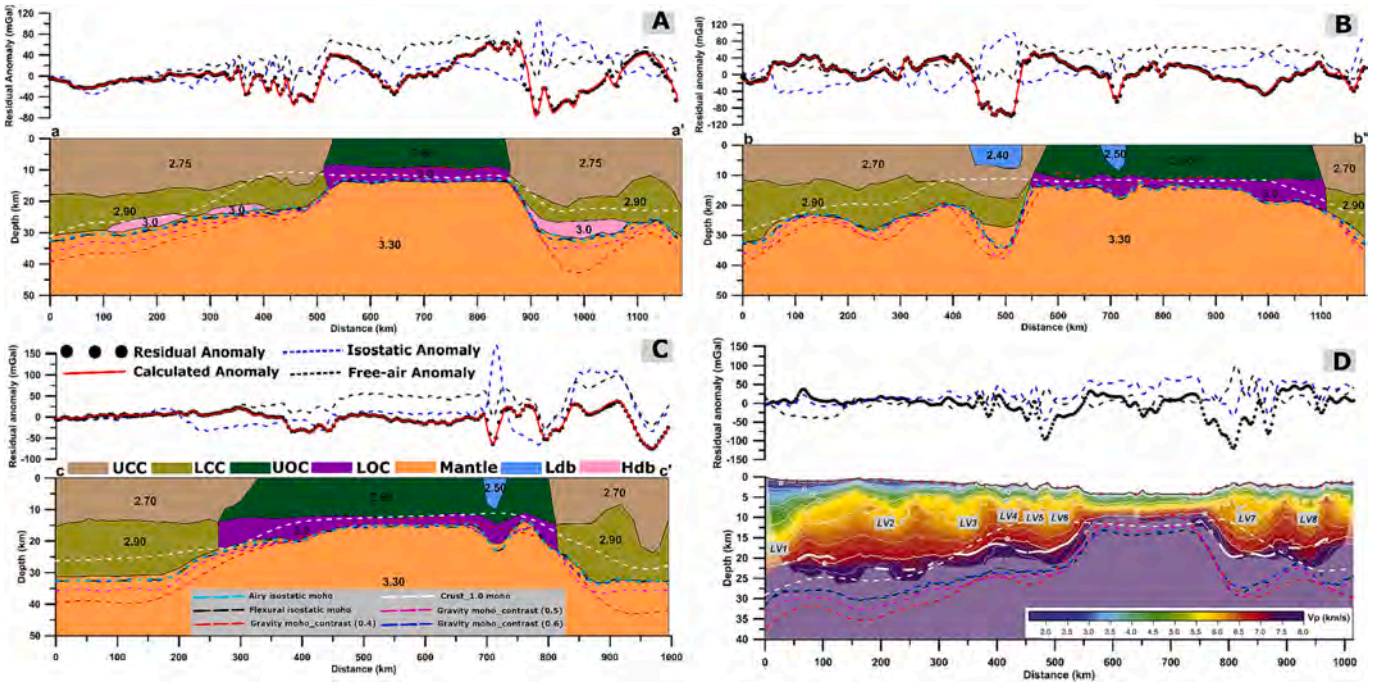

Fig. 8. Crustal structure with their density values derived from the gravity modelling (A) along the profile-1 (aa') (B) along the profile-2 (bb') (C) along the profile-3 (cc'). The locations of the profiles are shown in Fig. 3A (D) Final velocity model for the OBS profile (location shown in Fig. 3A) of Pichot et al. (2014) with our calculated Mohos and gravity anomalies. The velocity isocontours are drawn every 0.25 km/s.

upper and lower crustal layers are 9–32 km thick, with a density of 2.75 and 2.90 g/cm^3, respectively, whereas the oceanic upper & lower crust is 9–14 km thick, with a density of 2.80 and 3.0 g/cm^3 (between 550 and 850 km on the profile), and continental crust is reasonably thick (between 0 and 550 km; 850 and 1160 km on the profile). The Moho deepens swiftly from the PhuKhanha basin to the Southwest Sub-Basin (31 km depth), rises gently at the Southwest Sub-Basin (9–14 km depth), and then deepens again from the Southwest Sub-Basin to the Reed Bank, Palawan Island tectonic units (deepest 32 km in depth).

5.4.2. Profile-2 (bb')

Profile-2 (Fig. 3A) has a distance of 1180 km and goes through tectonic units of PhuKhanha basin, East Sub-Basin U1431, and Palawan Island. Seismic results of OBS2013-ZN and OBS2014-ZN (Ruan et al., 2016) were used to model the observed gravity anomaly. Significant faults served as tectonic unit borders and governed deep formations. The East Sub-basin has an oceanic crust, while the rest has a continental crust. The East sub-basin Bank is 8–14 km thick and has a density of 2.80 and 3.00 g/cm^3, upper and lower oceanic crust, respectively (Fig. 8B). Before the East sub-basin, the deep crustal thickness is visible at 9–34 km. From the continental slope (34 km depth on the Macclesfield Bank) to the sea basin, the Moho rises quickly (8–14 km depth).

5.4.3. Profile-3 (cc')

Profile-3 (Fig. 3A) runs the length of the SCS, passing through the continental margin of South China, SB, Northwest sub-basin, ODP1148, U1432, U1435, and the continental part of the Philippines. Seismic constraints from the OBS2006–3 (Wei et al., 2011) profile were used to model shallow and deeper sections with gravity anomalies. The subsurface structure under profile c-c' is the increasing weakening crust from continent to sea region, as seen in Fig. 8C. In the continental part of South China, the Moho is 33 km deep and progressively rises to around 19 km as it approaches the sea. This Moho towards the sea, we believe, is a thin continental crust, not an oceanic crust. The crust thickness ranges from 9 to 33 km, with 2.75 and 2.90 g/cm^3, respectively.

We added the interpreted seismic section (Fig. 8D), modified after Pichot et al. (2014). This seismic section was prepared based on the wide-angle refraction seismic data (location in Fig. 3A). Our gravity 2D models also show the same crustal architecture with little uncertainties of Mohos.

6. Discussion

A detailed study has been conducted using gravity and topography datasets to understand the crustal structure, isostatic nature, and

evolution of SCS. This study used various techniques, including power spectral analysis, gravity inversion, GTR, isostatic models, vertical tectonic stress calculation, and gravity modelling with seismic constraints. We have taken many constraints from previous studies of OBS and multi channel seismic sections (locations shown in Fig. 3A). The depth of the Moho is approximately 31.5 km, according to the spectral analysis of the Bouguer gravity anomaly (Fig. 3B), which is in good agreement with other findings (Franke et al., 2011; McIntosh et al., 2014; Pichot et al., 2014). Since our study covers the land and ocean regions, we used this depth as the average Moho depth for gravity inversion modelling. The variations in Moho of 8–48 km are shown by the gravity inversion models of various density contrasts (Fig. 4A-C), with the continent region and Continent-Ocean Transition (COT) boundary showing the deepest crust and the SCS basin showing the lowest values. As a result, the modification of the SCS basin is greatly influenced by the transition of the continental crust. According to reflection seismic data, the deep crust structure, detachment faults, and *syn*-rift sediments of the SCS continental margins are similar to those of the Iberia/Newfoundland margins, suggesting that mantle exhumation within the narrow COT (e.g., Ding and Li, 2016). The upwelled mantle may be shallowly buried beneath a very thin crust, according to reflection seismic sections and tomographic velocity structures revealed from the oceanic bottom seismic survey, even though the new IODP drilling results within COT of the northern SCS have not yet confirmed this theory (Sun et al., 2018). We also noticed the possible extension of the COT in the isostatic Moho from local and regional models (Fig. 6A, B), which range from 7 to 45 km and are near the gravity inversion Moho depths. Along with this, we tested the compensation depths of specific blocks from the GTR and VTS analyses (Fig. 7 & S4), revealing that the seamounts and reefs (Shuangfeng Basin: SB, Reed Bank: RB, Macclesfield Bank: MB) have a deeper compensation depth, while the other areas (Manila Trench: MT, Phu Khan Basin: PK, East Sub Basin: ESB) have the shallow depth of compensation. Finally, the gravity modelling performed from the chosen three profiles (Fig. 8) demonstrates the rifting, high density bodies at Moho in oceanic areas and the extension of the continental crust. It is clear how these continental edges differ from one another. The Basin and Range Province is reminiscent of the thinner southern SCS continent margin, which is wider than the Iberia-Newfoundland borders. Despite this, seismic profiles discovered the SCS COT with a width of 0–20 km, and our investigation is quite small. Although mantle exhumation within a restricted zone is possible when the lower crust is weak, this only provides a limited area for deep mantle and lower crustal material exhumation (Chenin and Beaumont, 2013). We propose that a weak lower crust controls the rift and breakup of the SCS. In the COT, magma-rich margins contain large volumes of intrusive and extrusive volcanic rocks, manifested as seaward dipping reflectors from volcanic flows (White et al., 1987). A high velocity lower crust (HVLC) is commonly attributed to magmatic underplating (Korenaga et al., 2000), intrusions in the lower crust at SCS, and Serpentinized mantle (White et al., 2008). The opening of the SCS could be a record of a mantle plume interacting with a rifting seafloor spreading system created along a continental boundary (Yu et al., 2018a, 2018b; Liu et al., 2004). Our gravity forward modelling along the profile-1 (Figs. 8A) demonstrate a high-density body at the lower crustal level, indicating a large rifted border with a significantly thinned and magmatically changed continental crust.

6.1. *Crustal architecture from gravity and its comparison with available seismic models*

The northern continental margin, the southern continental margin, and the oceanic basin can roughly be used to categorize the South China Sea. Over the SCS, numerous geological and geophysical studies have been conducted, including seismic surveys of the shallow mantle and crust (e.g., Qiu et al., 2001; Yan et al., 2001; Hayes and Nissen, 2005; Wang et al., 2006; Zhao et al., 2010; Ding et al., 2016). We compared our gravity-derived crustal thickness models to the crustal thickness estimates obtained from the seismic research in the SCS ocean basin to assess the robustness of the gravity modelling results. We compared the bathymetry, sediment thickness, and gravity derived Moho depth to the seismic measurements, paying particular attention to profiles that transect the SCS oceanic crust (Yan et al., 2001; Zhao et al., 2010; Qiu et al., 2011; Ruan et al., 2016); the Moho variations especially in oceanic crust, the results from gravity modelling and seismic analysis coincide fairly well (Fig. 8). The local inconsistency between the seismic and gravity models may have a few causes: (1) In some locations, the resolution of the sediment thickness data used in our gravity modelling may be lacking; (2) There may be lateral density variations along seismic profiles that were not taken into account in the gravity modelling; (3) Several seismic profiles cross the continental margin area, where the gravity edge effects from the assumed continental lithospheric ages may cause uncertainties. Both the gravity and seismic data provide significant constraints on the spatial variations of crustal and mantle properties of the SCS, even though the crustal thickness model derived from gravity would invariably differ from that of the crustal structure determined by seismicity due to the fundamental differences in data types and methodologies.

Distribution of thin crust from gravity, isostatic Moho, and gravity modelling (Figs. 4, 6, and 8) may identify oceanic crust within the SCS. In the eastern SCS, the extinct seafloor-spreading center was revealed to be significantly denser than the actual crust linked through underwater trenches. The Reed Bank, previously a portion of the MB continental block, is expected to contain a 22–28 km depth comparable to the Macclesfield Bank's current crustal thickness (Figs. 4 and 6). The south border of SCS in the west comprises thinning mainland crust fragments detached by a narrow zone that suffered greater units of thinning and stretching, according to crustal thicknesses using gravity modelling (Fig. 8). This region's crust was reduced to a greater extent than Reed Bank; crustal consistency is expected to be much smaller, reaching 10–20 km, according to seismic refraction modelling (Pichot et al., 2014). Compared to the moderately slight Palawan Island edge of SCS, the southern margin of SCS farther western exhibits thinning mainland crust that becomes increasingly broader on the DG border, measured by gravity inversion and isostatic models (Figs. 4, 6, and 8). The DG seems to relate to an extensive COT, 16–28 km, and Southward migration of the SCS ridge axis would predict a slightly thinner crust at the northern flank (Figs. 4 and 6). Because the initial break-up incident at the north of MB had not spread as distant westside, only one mainland break-up event occurred in the western segment of SCS. The summary of the Moho depths from gravity inversion, CRUST1.0, and Isostatic compensation of the selected nine blocks are shown in Table 1, along with the GTR and compensation depths.

Using a wide-angle seismic profile (OBS-2011-1), Huang et al. (2019) provided the seismic Moho and crustal structure of the South China Sea's northern margin. This OBS profile crosses very close to our gravity profile-1 (a-a'). The Moho varies from 12 to 25 km, 23 to 25 km beneath the Xisha Islands, 17 to 20 km across the Zhongsha Trough, and 12 to 14 km in the deep basin, according to the tomographic inversion results (Huang et al., 2019). These results agree with our gravity inversion (Fig. 4C) and gravity modelling (Fig. 8A) along the profile-1 (a-a'). To better understand the crustal structure in the central basin of the South China Sea (SCS), Ruan et al. (2016) used wide-angle seismic profiles (OBS2013-ZN, OBS2014-ZN) that cross the border (Zhongnan fault zone) between the east sub-basin and the southwest sub-basin. They showed that the Moho depths in the central basin range from 6 to 10 km, with the lowest values in the basin being 6–7 km and the highest in the thick sediment layers. Our gravity modelling profile −2 (b-b') crossed these seismic sections, and the gravity inversion results (Fig. 4C) well match this seismic section. Zhao et al. (2018) used 38 ocean-bottom seismometers placed in the South China Sea's central East subbasin to generate the P wave velocity models through forward and inverse modelling. This displayed four different types of crust, including the

thin, typical oceanic crust, the thick oceanic crust containing post-spreading volcanoes with large intrusive roots, and the thick oceanic crust with improved spreading features but no significant roots. They demonstrated that along the P-3, which crosses our gravity profile-2 (b-b'), the Moho varies from 9 to 13 km. This seismic section and our gravity model Moho have a very excellent correlation, and we added the high-density lower crustal bodies with intrusive roots and post-spreading volcanoes. Lester et al. (2013) employed the seismic reflection and coincident wide-angle ocean-bottom seismometer data to comprehend the crustal accretion in the Manila trench. Our gravity modelling profile-3 (c-c') somewhat crosses through this seismic section. In the Malina Trench area, the Moho varies between 10 and 20 km; it is high along the continental margin and low in the basin portion. The authors also demonstrated the lower crustal level's high velocity caused by volcanic intrusions and magmatic bodies. Our Moho depths from modelling (Fig. 8B) and gravity inversion (Fig. 4C) closely match those obtained from seismic sections. We also displayed the abrupt Moho dip at the trench region. To analyze the velocity structure of the incipient arc-continent collision along two trench perpendicular transects in the Bashi Strait between Taiwan and Luzon. Eakin et al. (2014) used multichannel seismic (MCS) reflection and wide-angle seismic datasets. At 20.5N, they discovered the subducting Malina trench and a hyper-extended continental crust 10–15 km thick. They demonstrated that the Moho varies along transect-1 by 10 to 18 km and that this transect follows our gravity profile-3 (c-c'). These results have a good correlation with our gravity modelling results. The other seismic experiments (Niu et al., 2014; Qiu et al., 2001; Qiu et al., 2011; Hung et al., 2021; Liu et al., 2014) have carried out a lot of seismic exploration in the SCS; however, these have lied mainly on the continental and ocean transition zone. Our gravity inversion matches these results, especially in the COT regions. However, some local differences may be due to the following factors: (1) resolution gaps between gravity inversion and seismic surveys (Wang et al., 2011); (2) lateral density variations along seismic profiles that were not considered in gravity modelling; and (3) ambiguities in the interpretation of seismic data (e.g., On the intersection point of OBS2011 and OBS2013–3, the diffraction pattern of the seismic data).

6.2. Isostatic compensation mechanism and magmatism

Effective elastic thickness (T_e), geoid-topography ratio (GTR), and vertical tectonic stress (VTS) are significant parameters commonly used to investigate the mechanism of isostatic compensation of volcanic stresses on oceanic lithosphere. The gravity and isostatic Moho are important in assessing the isostatic compensation mechanism of the area. The depth of compensation of selected blocks based on GTR values revealed that deeper compensation was found in Seamounts, reefs, and NCS, whereas shallow compensation was found in the sub-basins (Fig. 7 and Table 1). The difference of −5 to 6 km between the isostatic gravity Moho of the study region indicates the non-isostatic equilibrium of the crust; therefore, the isostatic state of the crust is determined using these two Mohos. Vertical Tectonic Stress (VTS; see supplementary information for details) reflects the movement in the crust subjected to isostatic change (Xuan et al., 2020). The VTS results (Fig. S5) demonstrate the negative values of most of the sea basin region and a positive value beneath the MB, RB, DG, and continental sections. The non-positive VTS measurements suggest that the area is under-compensated at the crustal part and that the crust is moving downwards vertically. The high crustal load inferred from positive VTS values in the Palawan, Luzon, and Taiwan Arcs, on the other hand, indicates crustal overcompensation and upward motion. Our models (Figs. 4, 6, and 8) suggest that the crustal thinning along the SCS basin may be caused by Isostasy, as evidenced by substantial positive gravity anomalies. This is also interpreted as lower crustal magmatism. Recent studies (Li et al., 2021; Pérez-Gussinyé, 2013; Sibuet et al., 2007; Pérez-Gussinyé et al., 2006) have shown the possibility of lower crustal magmatism based on MCS profiles. Following Lester et al. (2014), the high-velocity layer at the lower crustal level could be caused by mafic magmatism. The crustal thinning can result in upper mantle serpentinization or widespread magmatism, facilitating fragmentation (Pérez-Gussinyé et al., 2001). With the OBS refraction data (Lester et al., 2014), the velocity of the upper portion mantle (8.0 km/s) and high-rift basin are consistent with an unchanged topmost part of the mantle, which needs a hotter mantle (>500 °C) during rifting (Ulmer and Trommsdorff, 1995). Still, high lower-crust velocities illustrate the northern Continent-Ocean Transition (COT), resulting in a thick High-Velocity Belt (HVB) (Li et al., 2021). We also showed the high-density bodies at the lower crustal level in starting portion of gravity modelling profile-1 (Fig. 8A). This may be due to magmatic intrusion or underplating. Thermal subsidence proposed by Taylor and Hayes (1983) caused magma to travel uphill via fractures and usual faults near the margin of ZS, forming intrusions in the shallow crust during the post-spreading period. However, because the ZS is a thick continental domain, it has not been subjected to magmatism due to substantial tectonic extension and thinning. The thinned continental crust in the MGL0905–20 profile suggests post-rift volcanism intrusion (Fig. 9). Underplating is featured in MCS profiles(MGL0905–10 and MGL0905–20), cutting through the magnetic lineations (Fig. 9).

7. Conclusions

The combined analyses of bathymetry/elevation, geoid, and gravity, along with the seismic velocities, have shown novel information on the compensation mechanism, crustal structure, and tectonic past of the South China Sea from results of gravity, isostatic Moho, GTRs, Vertical Tectonic Stress, and 2-D gravity modelling. The gravity-derived Moho displays a decreasing depth towards the SCS center from continental borders, a buckled morphology from north to south over the Xisha Trough, Palawan, and the Philippines, and a sharp uplift of Macclesfield Bank and Reed bank. The Moho has a depth identical to the continental boundary beneath continental rift basins and continental margins backed through confirmation that SCS was formed from the Eurasian continent addition. As a result, the shallow Moho in the SCS's center implies the isostasy caused crustal thinning (strong positive gravity anomalies). Comparing the isostatic and gravity states to assess the crustal isostatic condition, Indo China, the SCS, Palawan, and the Philippines are compensated regions. The Moho should raise beneath the overcompensated Macclesfield Bank and Reed bank while becoming depressed beneath the undercompensated sub-basins. Crustal model constraints on the structure of the north-eastern SCS reveal a continental shelf with an extended crust of 20–28 km thick (Dongsha Rise). As previously documented in the north-eastern SCS, this crust, thinner than conventional continental crust but thicker than oceanic crust, gradually thins seaward. Based on these models, we deduce that the crust is different at the basin's center and that the continental crust is intruded by elongated volcanic structures away from the basin. The breakup happened after the crust and mantle lithosphere weakening, which might have prompted the ascending loosen-up of asthenospheric and subsequent seafloor spreading. We show that the crust in some parts of the SCS margin contains highly extended continental crust with interspersed volcanic zones, similar to the wide rifted margin observed throughout the rest of the SCS margin, using Mohos calculated using various methods and gravity forward modelling along with the profiles.

CRediT authorship contribution statement

A.V. Satyakumar: Conceptualization, Data curation, Visualization, Resources, Formal analysis, Investigation, Methodology, Software, Writing – original draft, Writing – review & editing. **Shuanggen Jin:** Supervision, Methodology, Validation, Writing – review & editing. **Virendra M. Tiwari:** Supervision, Methodology, Validation, Writing – review & editing. **Songbai Xuan:** Methodology, Validation, Writing – review & editing.

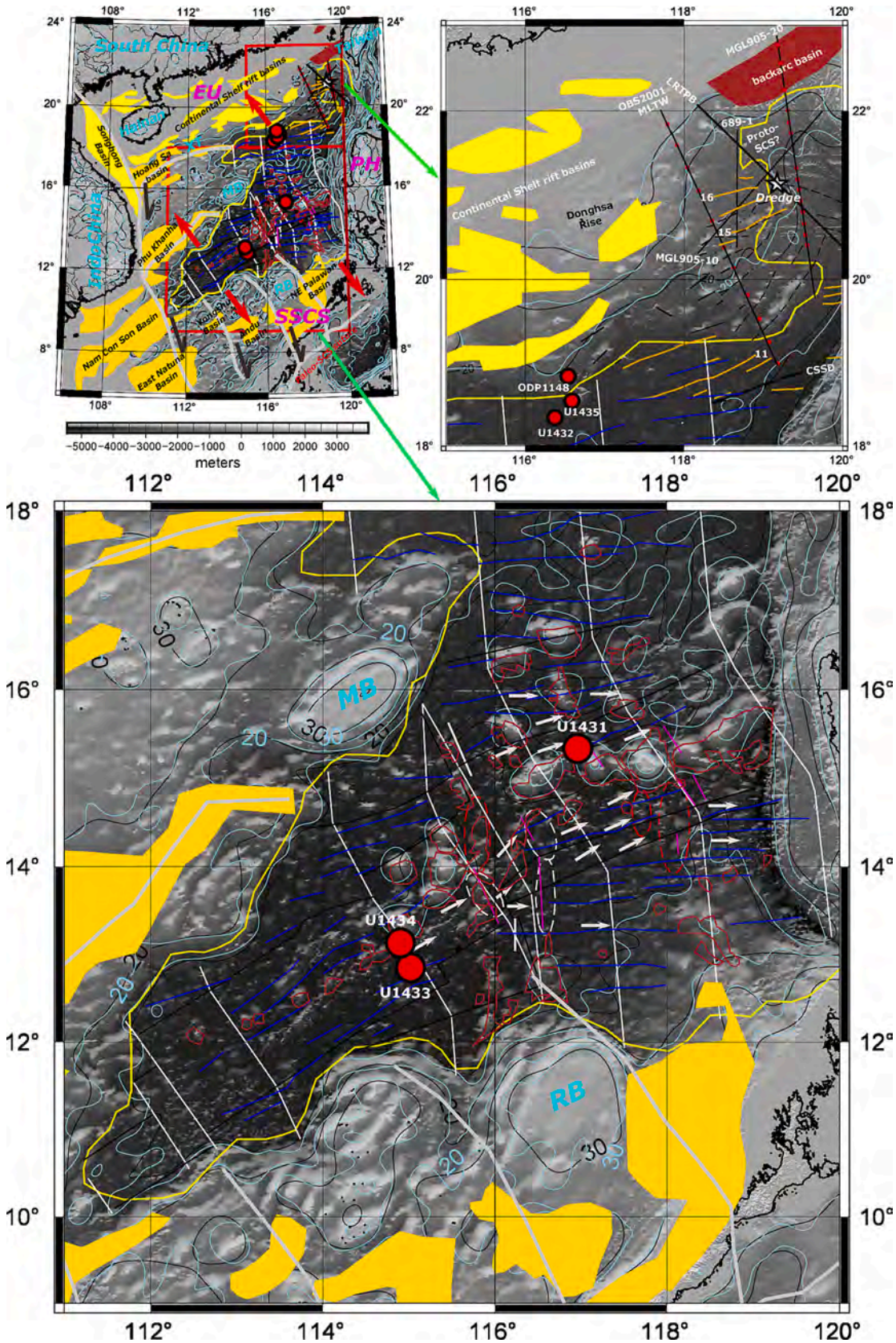

Fig. 9. Integration of all the previous seismic profiles, Chrons, Structural highs (elongated volcanic intrusions), Elongated depressions, Ridge axes, Underline uplifted, non-uplifted seafloor spreading features, OBS, Kinematic flow lines, magnetic lineaments, seafloor spreading direction, borehole locations, Extension directions, post spreading volcanism boundaries with our crustal depths. The Gravity Moho, Black and sky-blue solid lines, and Isostatic Moho are superposed on these features. The yellow and red shadows are the different major basins. (For interpretation of the references to colour in this figure legend, the reader is referred to the web version of this article.)

Author statement

We confirm that the manuscript has been read and approved by all named authors and that there are no other persons who satisfied the criteria for authorship but are not listed. We further confirm that the order of authors listed in the manuscript has been approved by all of us.

We understand that the Corresponding Author is the sole contact for the Editorial process. He is responsible for communicating with the other authors about progress, submissions of revisions and final approval of proofs.

Declaration of Competing Interest

The authors declare no competing interests.

Data availability

The datasets generated during the current study are available from the corresponding author (A.V. Satyakumar; satyageo41@gmail.com). The other global datasets, Bathymetry (https://www.gebco.net/data_and_products/gridded_bathymetry_data/), Free-air gravity (Sandwell et al., 2014), Sediment thickness (NCEI; Whittaker et al., 2013), Geoid (EGM2008; Pavlis et al., 2012) are freely available.

Acknowledgments

We are grateful to the Director, National Geophysical Research Institute (CSIR), Hyderabad, for approval to publish the work. The Bathymetry data is the GEBCO's worldwide topography model for land and ocean (GEBCO_2021; https://www.gebco.net/data_and_products/gridded_bathymetry_data/). The free-air gravity anomaly data is a 1' × 1' marine gravitational field model (Sandwell et al., 2014). Sediment thickness is available worldwide grid from the National Centers for Environmental Information (NCEI; Whittaker et al., 2013). The Geoid data is based on EGM2008, which signifies 2159 degree and order of spherical harmonics (Pavlis et al., 2012). Most images were produced using the Generic Mapping Tools (GMT; Wessel et al., 2013) software. AVSK is thankful to Mr. Bhaskar Illa for his help in extracting seismic velocities from the GyPSuM model. Shuanggen Jin supported by Experiments for Space Exploration Program of the Qian Xuesen Laboratory, China Academy of Space Technology (Grant No: TKTSPY-2020-06-02). We are grateful to Dr. Dominique Jault, Editor, and two *anonymous reviewers* for their careful reading of our manuscript and their many insightful comments and suggestions to improve the earlier version of the manuscript.

Appendix A. Supplementary data

Supplementary data to this article can be found online at https://doi.org/10.1016/j.pepi.2023.107107.

References

Abd-Elmotaal, H., 1993. VeningMeinesz Moho depths: traditional, exact, and approximated. Manuscr Geodaet 18, 171.
Abd-Elmotaal, H., 1995. Theoretical background of the VeningMeinesz isostatic model. In: Sunkel, H., Marson, I. (Eds.), Gravity and Geoid. IAG Symposium, 113. Springer, Berlin Heidelberg New York, pp. 268–277.
Bai, Y., Williams, S.E., Müller, R., Liu, Z., Hosseinpour, M., 2014. Mapping crustal thickness using marine gravity data: methods and uncertainties. Geophysics 79, G27–G36.
Barckhausen, U., Roeser, H.A., 2004. Seafloor spreading anomalies in the South China Sea revisited. In: Clift, P., Kuhnt, W., Wang, P., Hayes, D.E. (Eds.), Continente Ocean Interactions in the East Asian Marginal Seas, Geophysical Monograph Series. American Geophysical Union, pp. 121–125.
Barckhausen, U., Engels, M., Franke, D., Ladage, S., Pubellier, M., 2014. Evolution of the South China Sea: revised ages for breakup and seafloor spreading. Mar. Pet. Geol. 58, 599–611.
Bellingham, P., White, N., 2000. A general inverse method for modelling extensional sedimentary basins. Basin Res. 12, 219–226.
Bowin, C., 1983. Depth of principal mass anomalies contributing to the Earth's geoidal undulations and gravity anomalies. Mar. Geod. 7 (1), 61–100.
Braitenberg, C., Wienecke, S., Wang, Y., 2006. Basement structures from satellite-derived gravity field: South China Sea ridge. J. Geophys. Res. 111, B05407. https://doi.org/10.1029/2005JB003938.
Briais, A., Patriat, P., Tapponnier, P., 1993. Updated interpretation of magnetic anomalies and seafloor spreading stages in the South China Sea: implications for the tertiary tectonics of Southeast Asia. J. Geophys. Res. 98, 6299–6328.
Cameselle, A.L., Ranero, C.R., Franke, D., Barckhausen, U., 2017. The continent-ocean transition on the northwestern South China Sea. Basin Res. 29, 73–95. https://doi.org/10.1111/bre.12137.
Cao, J., Sun, J., Xu, H., Xia, S., 2014. Seismological features of the littoral fault zone in the Pearl River Estuary. Chinese J. Geophys. 57 (2), 498–508. https://doi.org/10.6038/cjg20140215.
Chen, M., Fang, J., Cui, R., 2018. Lithospheric structure of the South China Sea and adjacent regions: results from potential field modelling. Tectonophysics 726, 62–72. https://doi.org/10.1016/j.tecto.2018.01.021.
Chenin, P., Beaumont, C., 2013. Influence of Rheological Layering on the Formation of Offset Basins at Inherited Weak Zones during Continental Rifting: Effects of Stiff and Pliable Layers (Egu General Assembly).
Clift, P., Lin, J., 2001. Preferential mantle lithospheric extension under the South China margin. Mar. Pet. Geol. 18, 929–945.
Crough, S.T., 1978. Thermal origin of mid-plate hot-spots swells. Geophys. J. R Astron. Sot 55, 45l–469.
Ding, W., Li, J., 2016. Propagated rifting in the southwest subbasin, South China Sea: insights from analogue modelling. J. Geodyn. 100, 71–86.
Ding, W., Franke, D., Li, J., Steuer, S., 2013. Seismic stratigraphy and tectonic structure from a composite multi-channel seismic profile across the entire dangerous grounds, South China Sea. Tectonophysics 582, 162–176. https://doi.org/10.1016/j.tecto.2012.09.026.
Ding, W.W., Li, J.B., Clift, P., 2016. Spreading dynamics and sedimentary process of the Southwest-Sub-basin, South China Sea: constraints from multi-channel seismic data and IODP Expedition 349. J. Asian Earth Sci. 115, 97–113. https://doi.org/10.1016/j.jseaes.2015.09.013.
Ding, W., Sun, Z., Dadd, K., Fang, Y., Li, J., 2018. Structures within the oceanic crust of the central South China Sea basin and their implications for oceanic accretionary processes. Earth Planet. Sci. Lett. 488, 115–125. https://doi.org/10.1016/j.epsl.2018.02.011.
Eakin, D.H., McIntosh, K.D., Van Avendonk, H.J.A., Lavier, L., Lester, R., Liu, C.S., Lee, C. S., 2014. Crustal-scale seismic profiles across the Manila subduction zone: the transition from intraoceanic subduction to incipient collision. J. Geophys. Res. Solid Earth 119, 1–17.
Featherstone, W.E., 1997. On the use of the geoid in geophysics: a case study over the North West Shelf of Australia. ExplorGeophys 28 (2), 52. https://doi.org/10.1071/EG997052.GM027p0023.
Franke, D., Barckhausen, U., Baristeas, N., Engels, M., Ladage, S., Lutz, R., Montano, J., Pellejera, N., Ramos, E.G., Schnabel, M., 2011. The continent-ocean transition at the southeastern margin of the South China Sea. Mar. Pet. Geol. 28, 1187–1204. https://doi.org/10.1016/j.marpetgeo.2011.01.004.
Fyhn, M.B.W., Nielsen, L.H., Boldreel, L.O., Thang, L.D., Bojesen-Koefoed, J., et al., 2009. Geological evolution, regional perspectives and hydrocarbon potential of the northwest PhuKhanh Basin, offshore Central Vietnam. Mar. Pet. Geol. 26, 1–24.
GMSYS, 2000. Gravity/magnetic modelling software, version4.6. Northwest Geophysical Assoc Inc, U.S.A.
Gozzard, S., Kuszmir, N., Franke, D., Cullen, A., Reemst, P., Henstra, G., 2019. South China Sea crustal thickness and oceanic lithosphere distribution from satellite gravity inversion. Pet. Geosci. 25, 112–128.
Gruninger, W., 1990. ZurtopographischenReduktion der Schwere. Dissertation an der Universität Karlsruhe. Karlsruhe Technical University.
Guo, L., Meng, X., Chen, Z., Li, S., Zheng, Y., 2013. Preferential filtering for gravity anomaly separation. ComputGeosci 51, 247–254.
Hall, R., 2002. Cenozoic geological and plate tectonic evolution of SE Asia and the SW Pacific: computer-based reconstructions, model and animations. J. Asian Earth Sci. 20, 353–431. https://doi.org/10.1016/S1367-9120(01)00069-4.
Hall, R., Spakman, W., 2015. Mantle structure and tectonic history of SE Asia. Tectonophysics 658, 14–45. https://doi.org/10.1016/j.tecto.2015.07.003.
Haxby, W.F., Turcotte, D.L., 1978. On isostatic geoid anomalies. J. Geophys. Res. 83, 5473–5478.
Hayes, D.E., Nissen, S.S., 2005. The South China Sea margins: implications for rifting contrasts. Earth Planet. Sci. Lett. 237, 601–616. https://doi.org/10.1016/j.epsl.2005.06.017.
Hertz, H., 1895. Gesammelte Werke, 1, p. 155.
Holloway, N.H., 1982. North Palawan Block, Philippines-its relation to Asian mainland and role in evolution of South China Sea. AAPG Bull. 66 (9), 1355–1383. https://doi.org/10.1306/03B5A7A5-16D1-11D7-8645000102C1865D.
Hsu, S.K., Yeh, Y.C., Doo, W.B., Tsai, C.H., 2004. New bathymetry and magnetic lineations in the northernmost South China Sea and their tectonic implications. Mar. Geophys. Res. 25, 29–44. https://doi.org/10.1007/s11001-005-0731-7.
Huang, H., Qiu, X., Pichot, T., Klingelhoefer, F., Zhao, M., Wang, P., Hao, T., 2019. Seismic structure of the northwestern margin of the South China Sea: implication for asymmetric continental extension. Geophys. J. Int. 218 (2), 1246–1261. https://doi.org/10.1093/gji/ggz219.
Hung, T.D., Yang, T., Le, B.M., Yu, Y., Xue, M., Liu, B., Liu, C., Wang, J., Pan, M., Huong, P.T., Liu, F., Morgan, J.P., 2021. Crustal structure across the extinct mid ocean ridge in South China Sea from OBS receiver functions: insights into the

spreading rate and magma supply prior to the ridge cessation. Geophys. Res. Lett. 48 https://doi.org/10.1029/2020GL089755 e2020GL089755.
Hutchison, C.S., Vijayan, V.R., 2010. What are the Spratly Islands? J. Asian Earth Sci. 39, 371–385.
Hwang, C., 1999. A bathymetric model for the South China Sea from satellite altimetry and depth data. Mar. Geod. 22, 37–51.
Jian, Z., Larsen, H.C., Zarikian, C.A., the Expedition 368 Scientists, 2018. Expedition 368 Preliminary Report: South China Sea Rifted Margin. International Ocean Discovery Program. https://doi.org/10.14379/iodp.pr.368.2018.
Jin, S.G., Park, P., 2006. Strain accumulation in South Korea inferred from GPS measurements. Earth Planets Space 58 (5), 529–534. https://doi.org/10.1186/BF03351950.
Jong, J., Barker, S., 2014. The Sarawak bunguran fold belt: structural development in the context of South China Sea tectonics. In: Paper presented at the International Petroleum Technology Conference, Kuala Lumpur, Malaysia, December 2014.
Korenaga, J., Holbrook, W.S., Kent, G.M., Kelemen, P.B., Detrick, R.S., Larsen, H.C., Hopper, J.R., Dahl-Jensen, T., 2000. Crustal structure ofthe Southeast Greenland margin from joint refraction and reflection seismic tomography. J. Geophys. Res. 105 (B9), 21,591–21,614.
Kudrass, H.R., Wiedicke, M., Cepek, P., 1985. Mesozoic and Cenozoic rocks dredged from the South China Sea and their significance for plate-tectonic reconstructions. Mar. Pet. Geol. 3, 19–30.
Larsen, H.C., Mohn, G., Nirrengarten, M., Sun, Z., Stock, J., Jian, Z., et al., 2018. Rapid transition from continental breakup to igneous oceanic crust in the South China Sea. Nat. Geosci. 11 (10), 782–790. https://doi.org/10.1038/s41561-018-0198-1.
Laske, G., Masters, G., Ma, Z., Pasyanos, M.E., 2013. Update on CRUST1.0- A 1-degree global model of Earth's crust. Geophys. Res. Abstr. 15. Abstract EGU2013-2658. http://igppweb.ucsd.edu/~gabi/rem.html.
Lee, T.-Y., Lawver, L.A., 1995. Cenozoic plate reconstruction of Southeast Asia. Tectonophysics 251, 85–138.
Lester, R., McIntosh, K., 2012. Multiple attenuation in crustal-scale imaging: examples from the TAIGER marine reflection data set. Mar.Geophys. Res. 33 (4), 289–305.
Lester, R., McIntosh, K., Van Avendonk, H.J.A., Lavier, L., Liu, C.S., Wang, T.K., 2013. Crustal accretion in the Manila trench accretionary wedge at the transition from subduction to mountain-building in Taiwan. Earth and Planet. Sci. Lett. 375, 430–440. https://doi.org/10.1016/j.epsl.2013.06.007.
Lester, R., Van Avendonk, H.J.A., McIntosh, K., Lavier, L., Liu, C.-S., Wang, T.-K., Wu, F., 2014. Rifting andmagmatismin the northeastern South China Sea fromwide-angle tomography and seismic reflection imaging. J. Geophys. Res. 119, 2305–2323. https://doi.org/10.1002/2013JB010639.
Li, C., Shi, X., Zhou, Z., Li, J., Geng, J., Chen, B., 2010. Depths to the magnetic layer bottom in the South China Sea area and their tectonic implications. Geophys. J. Int. 182, 1229–1247. https://doi.org/10.1111/j.1365-246X.2010.04702.x.
Li, C.F., Xu, X., Lin, J., Sun, Z., Zhu, J., Yao, Y., Zhao, X., Liu, Q., Kulhanek, D.K., Wang, J., 2014. Ages and magnetic structures of the South China Sea constrained by deep tow magnetic surveys and IODP expedition 349. Geochem. Geophys. Geosyst. 15, 4958–4983.
Li, C.F., Lin, J., Kulhanek, D.K., Williams, T., Bao, R., Briais, A., et al., 2015. Expedition 349 summary. In: Li, C.F., Lin, J., Kulhanek, D.K., the Expedition 349 scientists (Eds.), Proceedings of the International Ocean Discovery Program, 349: South China Sea Tectonics. International Ocean Discovery Program, College Station, TX. https://doi.org/10.14379/iodp.proc.349.101.2015.
Li, Y., Huang, H., Grevemeyer, I., Qiu, X., Zhang, H., Wang, Q., 2021. Crustal structure beneath the Zhongsha Block and the adjacent abyssal basins, South China Sea: new insights into rifting and initiation of seafloor spreading. Gondwana Res. 99, 53–76. https://doi.org/10.1016/j.gr.2021.06.015.
Liu, M., Cui, X., Liu, F., 2004. Cenozoic rifting and volcanism in eastern China: a mantle dynamic link to the Indo-Asian collision? Tectonophysics 393 (1), 29–42.
Liu, C., Hua, Q., Pei, Y., Yang, T., Xia, S., Xue, M., Le, B.M., Huo, D., Liu, F., Huang, H., 2014. Passive-Source Ocean bottom seismograph (OBS) array experiment in South China Sea and data quality analyses. Chin. Sci. Bull. 59, 4524–4535. https://doi.org/10.1007/s11434-014-0369-4.
Lowry, A.R., Smith, R.B., 1994. Flexural rigidity of the Basin and Range-Colorado Plateau–Rocky Mountain transition from the coherence analysis of gravity and topography. J. Geophys. Res. 20, 99–123.
Mazur, S., Green, C., Stewart, M.G., Whittaker, J.M., Williams, S., Bouatmani, R., 2012. Displacement along the Red River Fault constrained by extension estimates and plate reconstructions. Tectonics 31 (5), 1–22. https://doi.org/10.1029/2012TC003174.
McIntosh, K., Lavier, L., van Avendonk, H., Lester, R., Eakin, D., Liu, C.S., 2014. Crustal structure and inferred rifting processes in the northeast South China Sea. Mar. Pet. Geol. 58, 612–626.
McIntosh, K., Van Avendonk, H., Lavier, L., Lester, R., Eakin, D., Wu, F., Liu, C.-S., 2013. Inversion of a hyper-extended rifted margin in thesouthern Central Range of Taiwan. Geology 41 (8), 871–874.
McKenzie, D.P., Watts, A.B., Parsons, B., Roufouse, M., 1980. Platform of mantle convection beneath the Pacific Ocean. Nature 288, 442–446.
Mishra, D.C., Pederson, L.B., 1982. Statistical analysis of potential fields from sub surface reliefs. Geoexploration 19, 247–265.
Monnereau, M., Cazenave, A., 1988. Variation of the apparent compensation depth of hot spot swells with age of plate. Earth Planet. Sci. Lett. 91, 179–197.
Moritz, H., 1990. The inverse VeningMeinesz problem in isostasy. Geophys. J. Int. 102, 733–738.
Morley, C.K., 2002. A tectonic model for the tertiary evolution of strike slip faults and rift basins in SE Asia. Tectonophysics 347 (4), 189–215. https://doi.org/10.1016/S0040-1951(02)00061-6.
Nadai, A., Hodge, P.G., 1963. Theory of flow and fracture of solids. J. Appl. Mech. 230640.
Nissen, S.S., Hayes, D.E., Buhl, P., Diebold, J., Bochu, Y., ZengW, Chen Y., 1995. Deep penetration seismic soundings across the northern margin of the South China Sea. J. Geophys. Res. Solid Earth 100, 22407–22433.
Niu, X., Wei, X., Ruan, A., Wu, Z., 2014. Comparison of inversion method of wide-angle ocean bottom seismometer profile: a case study of profile OBS973-2 across Liyue Bank in the South China Sea. Chin. J. Geophys. 57, 607–618. https://doi.org/10.1002/cjg2.20127.
Oldenburg, D.W., 1974. The inversion and interpretation of gravity anomalies. Geophysics 39, 526–536.
Parker, R.L., 1973. The rapid calculation of potential anomalies. Geophys. J. R. Astron. Soc. 31, 447–455.
Pavlis, N.K., Holmes, S.A., Kenyon, S.C., Factor, J.K., 2012. The development and evaluation of the Earth Gravitational Model 2008 (EGM2008). J. Geophys. Res. 117 https://doi.org/10.1029/2011JB008916 (B04406).
Pérez-Gussinyé, M., 2013. A tectonic model for hyperextension at magma-poor rifted margins: an example from the West Iberia-Newfoundland conjugate margins. Geo Soc. Lond. Spec. Pub. 369 (1), 403–427. https://doi.org/10.1144/SP369.19.
Pérez-Gussinyé, M., Reston, T.J., Morgan, J.P., 2001. Serpentinization and magmatism during extension at non-volcanic margins: The effect of initial lithospheric structure. In: Wilson, R.C.L., et al. (Eds.), Non-Volcanic Rifting of Continental Margins: A Comparison of Evidence from Land and Sea. Geol Soc Spec Pub, 187, pp. 551–576. London UK.
Pérez-Gussinyé, M., Morgan, J.P., Reston, T.J., Ranero, C.R., 2006. The rift to drift transition at non-volcanic margins: insights from numerical modelling. Earth Planet. Sci. Lett. 244 (1–2), 458–473. https://doi.org/10.1016/j.epsl.2006.01.059.
Pichot, T., Delescluse, M., Chamot-Rooke, N., Pubellier, M., Qiu, Y., Meresse, F., et al., 2014. Deep crustal structure of the conjugate margins of the SW South China Sea from wide-angle refraction seismic. Mar. Pet. Geol. 58, 627–643.
Pigott, J.D., Ru, K., 1994. Basin superposition on the northern margin of the South China Sea. Tectonophysics 235, 27–50.
Qiu, X., Ye, S., Wu, S., Shi, X., Zhou, D., Xia, K., Flueh, E.R., 2001. Crustal structure across the Xisha trough, northwestern South China Sea. Tectonophysics 341, 179e193.
Qiu, X., Zhao, M., Ao, W., Lv, C., Hao, T., You, Q., et al., 2011. OBS survey and crustal structure of the Southwest Sub-basin and Nansha Block, South China Sea (in Chinese with English abstract). Chin. J. Geophys. Chin. 54 (12), 3117–3128. https://doi.org/10.3969/j.issn.0001-5733.2011.12.012.
Qiu, X., Ming-hui, Zhao, Xu, Hui-long, Jia-biao, Li, Ai-guo, Ruan, Tian-yao, Hao, Qing-yu, You, 2012. Important processes of deep seismic surveys in the South China Sea: retrospection and expectation. J. Trop. Ocean 31 (3), 1–9. https://doi.org/10.3969/j.issn.1009-5470.2012.03.001.
Replumaz, A., Tapponnier, P., 2003. Reconstruction of the deformed collision zone between India and Asia by backward motion of lithospheric blocks. J. Geophys. Res. 108 (B6), 2285. https://doi.org/10.1029/2001JB000661.
Ruan, A., Wei, X., Niu, X., Zhang, J., Dong, C., Wu, Z., Wang, X., 2016. Crustal structure and fracture zone in the central basin of the South China Sea from wide angle seismic experiments using obs. Tectonophysics 688, 1–10. https://doi.org/10.1016/j.tecto.2016.09.022.
Sandwell, D.T., MacKenzie, K.R., 1989. Geoid height versus topography for oceanic plateaus and swells. J. Geophys. Res. 94, 7403–7418.
Sandwell, D.T., Smith, W.H.F., 2001. Bathymetric estimation. In: Fu, L.-L., Cazenave, A. (Eds.), Satellite Altimetry and Earth Sciences. Elsevier, New York, pp. 441–457.
Sandwell, D.T., Muller, R.D., Smith, W.H.F., Garcia, E., Francis, R., 2014. New global marine gravity model from CryoSat-2 and Jason-1 reveals burie tectonic structure. Science 346, 65–67.
Schlüter, H.U., Hinz, K., Block, M., 1996. Tectono-stratigraphic terranes and detachment faulting of the South China Sea and Sulu Sea. Mar. Geol. 130, 39–78.
Shi, X., Zhou, D., Zhang, Y., 2000. Lithospheric thermal-rheological structures of the continental margin in the northern South China Sea. ChinSciBull 45, 2107–2112.
Sibuet, J.-C., Srivastava, S., Manatschal, G., 2007. Exhumed mantle-forming transitional crust in the Newfoundland-Iberia rift and associated magnetic anomalies. J. Geophys. Res. 112, B06105 https://doi.org/10.1029/2005JB003856.
Sibuet, J.-C., Yeh, Y.-C., Lee, C.-S., 2016. Geodynamics of the South China Sea. Tectonophysics 692, 98–119.
Smith, W.H.F., Sandwell, D.T., 1997. Global sea floor topography from satellite altimetry and ship depth soundings. Science 277, 1956–1962.
Spector, A., Grant, F.S., 1970. Statical models for interpretating aeromagnetic data. Geophysics 35, 293–302.
Su, D., White, N., McKenzie, D., 1989. Extension and subsidence of the Pearl River mouth basin, northern South China Sea. Basin Res. 2, 205–222.
Sun, Z., Stock, J., Klaus, A., the Expendition 367 Scientists, 2018. Expedition 367 Preliminary Report: South China Sea Rifted Margin. International Ocean Discovery Program. https://doi.org/10.14379/iodp.pr.367.2018.
Talwani, M., Worzel, J., Landisman, M., 1959. Rapid gravity computations for two dimensional bodies with application to the Mendocino submarine fracture zone. J. Geophys. Res. 64 (1), 49–59. https://doi.org/10.1029/JZ064i001p00049.
Tapponnier, P., Peltzer, G., Le Dain, A.Y., Armigo, R., Cobbold, P., 1982. Propagating extrusion tectonics in Asia: new insights from simple experiments with plasticine. Geology 10, 611–616. https://doi.org/10.1130/0091-7613.
Tapponnier, P., Peltzer, G., Armijo, R., 1986. On the mechanics of collision between India and Asia. In: Coward, M., Ries, A.C. (Eds.), Collision Tectonics, 19. Geol Soc London, pp. 115–157. https://doi.org/10.1144/GSL.SP.1986.019.01.07.

Taylor, B., Hayes, D., 1983. Origin and history of the South China Sea basin. In: The Tectonic and Geologic Evolution of Southeast Asian Seas and Islands. Geophysical Monograph Series, 27, pp. 23–56. https://doi.org/10.1029/GM027p0023.
Thies, K., Mansor, A., Hamdon, M., Bishkel, R., Boyer, J., Tearpock, D., 2005. Structural and stratigraphic development of extensional basins: A case study offshore deepwater Sarawak and northwest Sabah, Malaysia. In: AAPG Search and Discovery Article #10103, AAPG Annual Convention, June 19-22, Calgary, Alberta, Canada.
Ulmer, P., Trommsdorff, V., 1995. Serpentine stability to mantle depths and subduction-related magmatism. Science 268, 858–861.
VeningMeinesz, F.A., 1940. The Earth's Crust Deformation in the East Indies. KoninklijkeNederlandsche Akademie van wetenschappen.
Wang, P., et al., 2000. Proceedings of the Ocean Drilling Program: Initial Reports, vol. 184. Ocean Drill. Program, College Station, Tex. Available at. http://www-odp.tamu.edu/publications/184_IR/184ir.htm.
Wang, Y., Xu, H., Zhan, J., 2001. High resolution bathymetry of China seas and their surroundings. Chin. Sci. Bull. 46, 1661–1664.
Wang, Q.S., An, Y.L., Zhang, C.J., Jiang, F.Z., 2003. Gravitology. Seismological Press, Beijing, pp. 17–33.
Wang, T.K., Chen, M.K., Lee, C.S., Xia, K., 2006. Seismic imaging of the transitional crust across the north-eastern margin of the South China Sea. Tectonophysics 412, 237–254.
Wang, Q.S., Teng, J.W., Zhang, Y.Q., ZhangXM, Yang H., 2009a. The crustal structure and gravity isostasy in the middle western Sichuan area. Chin. J. Geophys. 52 (2), 579–583 (in Chinese with English abstract).
Wang, Y.J., Zhang, Y.Z., Zhao, G.C., Fan, W.M., Xiao, X.P., Zhang, F.F., Zhang, A.M., 2009b. Zircon U–Pb geochronological and geochemical constraints on the petrogenesis of the Taishansanukitoids (Shandong): implications for Neoarchean subduction in the Eastern Block, North China Craton. Precambrian Res. 174 (3–4), 273–286.
Wang, T., Lin, J., Tucholke, B., Chen, Y.J., 2011. Crustal thickness anomalies in the North Atlantic Ocean basin from gravity analysis. Geochem. Geophys. Geosyst. 12. Q0AE02.
Watts, A.B., 2001. Isostasy and Flexure of the Lithosphere. Cambridge University Press, Cambridge.
Wei, X.D., Ruan, A.G., Zhao, M.H., Qiu, X.L., Li, J.B., Zhu, J.J., Wu, Z.L., Ding, W.W., 2011. A wide-angle OBS profile across the Dongsha uplift and Chaoshan depression in the mid-northern South China Sea. Chin. J. Geophys. 54 (6), 1149–1160.
White, R.S., Spence, G.D., Fowler, S.R., McKenzie, D.P., Westbrook, G.K., Bowen, A.N., 1987. Magmatism at rifted continental margins. Nature 330 (6147), 439–444.
Wei, X.D., Ruan, A.G., Zhao, M.H., Qiu, X., Wu, Z., Niu, X., 2015. Shear wave velocity structure of Reed Bank, southern continental margin of the South China Sea. Tectonophysics 644–645, 151–160.
Wessel, P., Smith, W.H.F., Scharroo, R., Luis, J.F., Wobbe, F., 2013. Generic Mapping Tools: Improved version released. EOS Trans. AGU 94, 409–410.
White, R.S., Smith, L.K., Roberts, A.W., Christie, P.A.F., Kusznir, N.J., 2008. Lower-crustal intrusion on the North Atlantic continentalmargin. Nature 452 (7186), 460–464.
Whittaker, J., Goncharov, A., Williams, S., Muller, R.D., Leitchenkov, G., 2013. Global sediment thickness data set updated for the Australian-Antarctic Southern Ocean. Geochem. Geophys. Geosyst. 14, 3297–3305. https://doi.org/10.1002/ggge.20181.
Wu, J., Suppe, J., 2018. Proto-South China Sea plate tectonics using subducted slab constraints from tomography. J. Earth Sci. 29 (6), 1304–1318. https://doi.org/10.1007/s12583-017-0813-x.
Wu, Z.L., Li, J.B., Ruan, A.G., Lou, H., Ding, W.W., Niu, X.W., Li, X.B., 2011. Crustal structure of the northwestern sub-basin, South China Sea: results from a wide-angle seismic experiment. Sci. China Earth Sci. 55 (1), 159–172. https://doi.org/10.1007/s11430-011-4324-9.
Wu, J., Suppe, J., Lu, R., Kanda, R., 2016. Philippine Sea and East Asian plate tectonics since 52 Ma constrained by new subducted slab reconstruction methods. J. Geophys. Res. Solid Earth 121, 4670–4741. https://doi.org/10.1002/2016JB012923.
Xuan, S., Jin, S., Chen, Y., 2020. Determination of the isostatic and gravity Moho in the East China Sea and its implications. J. Asian Earth Sci. 187, 104098. https://doi.org/10.1016/j.jseaes.2019.104098.
Yan, P., Di, Z., Zhaoshu, L., 2001. A crustal structure profile across the northern continental margin of the South China Sea. Tectonophysics 338 (1), 1–21.
Yan, P., Deng, H., Liu, H., Zhang, Z., Jiang, Y., 2006. The temporal and spatial distribution of volcanism in the South China Sea region. J. Asian Earth Sci. 27, 647–659.
Yan, Q., Shi, X., Castillo, P.R., 2014. The late Mesozoic-Cenozoic tectonic evolution of the South China Sea: a petrologic perspective. J. Asian Earth Sci. 85, 178–201. https://doi.org/10.1016/j.jseaes.2014.02.005.
Yeh, Y.-C., Hsu, S.-K., 2004. Crustal structures of the northernmost South China Sea: seismic reflection and gravity modeling. Mar. Geophys. Res. 25, 45–61.
Yeh, Y.-C., Hsu, S.-K., Doo, W.-B., Sibuet, J.-C., Liu, C.-S., Lee, C.-S., 2012. Crustal features of the northeastern South China Sea: insights fromseismic and magnetic interpretations. Mar. Geophys. Res. 33 (4), 307–326.
Yu, Z., Li, J., Ding, W., Zhang, J., Ruan, A., Niu, X., 2017a. Crustal structure of the Southwest Subbasin, South China Sea, from wide-angle seismic tomography and seismic reflection imaging. Mar. Geophys. Res. 38 (1–2), 85–104. https://doi.org/10.1007/s11001-016-9284-1.
Yu, C.H., Zhao, J.F., Shi, X.B., et al., 2017b. Sediment density correction of gravity anomaly in the South China Sea and its significance to analyze regional tectonic characteristics. Chin. J. Geophys. 60 (8), 3151–3166. https://doi.org/10.6038/cjg0170822 (in Chinese).
Yu, M., Yan, Y., Huang, C.-Y., Zhang, X., Tian, Z., Chen, W.-H., Santosh, M., 2018a. Opening of the South China Sea and upwelling of the Hainan Plume. Geophys. Res. Lett. 45, 2600–2609.
Yu, J., Yan, P., Wang, Y., Zhang, J., Qiu, Y., Pubellier, M., Delescluse, M., 2018b. Seismic evidence for tectonically dominated seafloor spreading in the Southwest Subbasin of the South China Sea. Geochem. Geophys. Geosyst. 19, 3459–3477. https://doi.org/10.1029/2018GC007819.
Zahirovic, S., Seton, M., Müller, D.R., 2014. The Cretaceous and Cenozoic tectonic evolution of Southeast Asia. J. Geophys Res. Solid Earth 5 (1), 227–273. https://doi.org/10.5194/se-5-227-2014.
Zeyen, H., Fernàndez, M., 1994. Integrated lithospheric modeling combining thermal, gravity, and local isostasy analysis: application to the NE Spanish geotransect. J. Geophys. Res. 99 (B9), 89–102. https://doi.org/10.1029/94JB00898, 18.
Zhang, Z., Wang, Y., 2007. Crustal structure and contact relationship revealed from deep seismic sounding data in South China. Phys. Earth Planet. Inter. 165, 114–126.
Zhang, G.L., Luo, Q., Zhao, J., Jackson, M.G., Guo, L.S., Zhong, L.F., 2018. Geochemical nature of sub-ridge mantle and opening dynamics of the South China Sea. Earth Planet. Sci. Lett. 289, 145–155. https://doi.org/10.1016/j.epsl.2018.02.040.
Zhao, M., He, E., Sibuet, J.-C., Sun, L., Qiu, X., Tan, P., Wang, J., 2018. Postseafloor spreading volcanism in the central east South China Sea and its formation through an extremely thin oceanic crust. Geochem. Geophys. Geosyst. 19, 621–641. https://doi.org/10.1002/2017GC007034.
Zhao, M., Qiu, X., Xia, S., Xu, H., Wang, P., Wang, T.K., Lee, C.-S., Xia, K., 2010. Seismic structure in the northeastern South China Sea: S-wave velocity and Vp/Vs ratios derived from three-component OBS data. Tectonophysics 480, 183–197. https://doi.org/10.1016/j.tecto.2009.10.004.
Zhao, F., Alves, T.M., et al., 2016. Prolonged post-rift magmatism on highly extended crust of divergent continental margins (Baiyun Sag, South China Sea). Earth Planet. Sci. Lett. 445, 79–91.
Zhou, D., Sun, Z., Chen, H.Z., Xu, H.H., Wang, W.Y., Pang, X., Cai, D.S., Hu, D.K., 2008. Mesozoic paleogeography and tectonic evolution of South China Sea and adjacent areas in the context of Tethyan and paleo-Pacific interconnections. Island Arc 17 (2), 186–207. https://doi.org/10.1111/j.1440-1738.2008.00611.x.
Zhu, J., Xu, H., Qiu, X., Ye, C., Li, S., Somerville, I., 2017. Crustal structure and rifting of the northern South China Sea margin: evidence from shoreline-crossing seismic investigations. Geol. J. 53, 2065–2083. https://doi.org/10.1002/gj.3034.